

Driving classical Wolf-Rayet winds: A Γ - and Z -dependent mass-loss

Andreas A. C. Sander,^{1*} J. S. Vink,¹ and W.-R. Hamann²

¹*Armagh Observatory and Planetarium, College Hill, Armagh BT61 9DG, Northern Ireland, UK*

²*Institut für Physik & Astronomie, Universität Potsdam, Karl-Liebknecht-Str. 24/25, 14476 Potsdam, Germany*

Accepted 2019 October 28. Received 2019 October 28; in original form 2019 August 06

ABSTRACT

Classical Wolf-Rayet (WR) stars are at a crucial evolutionary stage for constraining the fates of massive stars. The feedback of these hot, hydrogen-depleted stars dominates their surrounding by tremendous injections of ionizing radiation and kinetic energy. The strength of a WR wind decides the eventual mass of its remnant, likely a massive black hole. However, despite their major influence and importance for gravitational wave detection statistics, WR winds are particularly poorly understood. In this paper, we introduce the first set of hydrodynamically consistent stellar atmosphere models for classical WR stars of both the carbon (C) and nitrogen (N) sequence, i.e. WC and WN stars, as a function of stellar luminosity-to-mass ratio (or Eddington Gamma), and metallicity. We demonstrate the inapplicability of the CAK wind theory for classical WR stars and confirm earlier findings that their winds are launched at the (hot) iron (Fe) opacity peak. For $\log Z/Z_{\odot} > -2$, Fe is also the main accelerator throughout the wind. Contrasting previous claims of a sharp lower mass-loss limit for WR stars, we obtain a smooth transition to optically thin winds. Furthermore, we find a strong dependence of the mass-loss rates on Eddington Γ , both at solar and sub-solar metallicity. Increases in WC carbon and oxygen abundances turn out to slightly reduce the predicted mass-loss rates. Calculations at subsolar metallicities indicate that below the metallicity of the SMC, WR mass-loss rates decrease much faster than previously assumed, potentially allowing for high black hole masses even in the local universe.

Key words: stars: Wolf-Rayet – stars: atmospheres – stars: fundamental parameters – stars: early-type – stars: mass-loss – stars: winds, outflows

1 INTRODUCTION

Among the highly influential massive stars, Wolf-Rayet (WR) stars are a rare but particularly important class. Their outstanding spectral appearance with huge emission lines dominating their optical spectrum allowed not only their discovery back in the 19th century (Wolf & Rayet 1867), but also led to the idea that these stars have strong stellar winds (Beals 1929), long before this was discovered to be inherent to the overwhelming majority of hot and massive stars.

By definition, WR stars are a spectroscopic category of stars with strong emission lines. As this can include very different types of objects, the term “classical Wolf-Rayet” (cWR) stars has been introduced in the more recent years, describing the hydrogen-depleted WR stars, associated with the end-points of the evolution of the most massive stars (e.g. Crowther 2007). Even today it is not yet known whether cWR stars produce supernovae (SNe) Ibc (e.g. Yoon et al. 2012; Groh et al. 2013), or if they collapse directly into a black hole (BH), i.e. without a visible display. In the latter case, SNe Ibc might generally be associated with lower mass binary ‘stripped’ helium (He) stars (e.g. Eldridge et al. 2013) which

may or may not have a WR-type spectral appearance depending on their mass-loss rate \dot{M} . Even in this case, stellar wind mass loss during the He-burning phase is the key to removing the remaining hydrogen (H), in order to produce H-free Ibc SNe (e.g. Gilkis et al. 2019).

The final phases of massive star evolution over a wide mass range – for both single and binary evolution – heavily rely on the assumed He star mass-loss rates. The need for a proper understanding of He star mass loss has become even more prevalent after the discovery of gravitational waves (GWs) from merging BHs, such as GW 150914. Abbott et al. (2016) showed that the evolutionary scenarios towards collapse depend heavily on the assumed WR mass loss, and only if a metallicity (Z) dependence (Vink & de Koter 2005) is accounted for, the ‘heavy’ nature of GW 150914 becomes possible (Belczynski et al. 2010; Abbott et al. 2016).

The Z -dependent mass-loss rates of Vink & de Koter (2005) which have for example been used to constrain the history of the massive BHs, were only computed for two ‘prototypical’ late-type WR stars with relatively low effective temperatures (on the order of 50 000 K). So far, a general theoretical prescription for WR stars does not exist. Therefore, most stellar evolutionary models (e.g. Georgy et al. 2012; Chen et al. 2015; Grassitelli et al. 2016; Renzo et al. 2017; Limongi & Chieffi 2018) still rely on empirical

* E-mail: Andreas.Sander@armagh.ac.uk

\dot{M} recipes, such as Nugis & Lamers (2000). Whilst these recipes might provide meaningful constraints inside the regime for which they were derived, they may fail substantially outside (Vink 2017).

Our aim is thus to alleviate current shortcomings by computing the up to date most-sophisticated hydro-dynamically consistent cWR wind models. Until now, only one such model has been constructed for a WC5 star by Gräfener & Hamann (2005, hereafter GH2005), highlighting the challenge in this task. In recent years, Sander et al. (2015, 2017, 2018) developed a new hydrodynamical version of the PoWR stellar atmosphere code (Hamann & Koesterke 1998; Gräfener et al. 2002) which is ideally suited for this task. One of the key advantages of this method is that it not only includes multi-line scatterings (as do Monte Carlo methods, e.g. Abbott & Lucy 1985; Vink et al. 1999; Noebauer & Sim 2015) but it also performs the radiative transfer in the co-moving frame (CMF), without any reliance on the Sobolev approximation.

Traditionally, WR winds are believed to be radiatively driven, making them similar to OB star winds. Still, the concepts successfully applied in the regime of OB supergiants, especially the so-called CAK theory (named after Castor, Abbott & Klein 1975) and its later extensions and modifications (‘mCAK’) (e.g. Friend & Abbott 1986; Pauldrach et al. 1986; Kudritzki & Puls 2000) turned out to be insufficient in describing the more dense WR winds (e.g. Lamers & Leitherer 1993), presumably due to the inherent restriction to single scattering. While the fact that the luminosities and terminal wind velocities of OB and WR stars are quite similar was one of the arguments for radiative driving in the first place, their empirical \dot{M} measured from radio and/or deduced from stellar atmosphere models are about an order of magnitude higher (e.g. Schmutz et al. 1989; Nugis & Lamers 2000; Puls et al. 2008). Over the years, insight has grown thanks to the understanding of WR ionization stratification (Lucy & Abbott 1993), photon trapping (Owocki 1994), and multi-line scattering (e.g. Gayley et al. 1995).

By studying the conditions at the sonic point, Nugis & Lamers (2002) concluded that WR winds with their high \dot{M} could potentially be launched in the optically thick regime due to an iron opacity bump. The idea of launching WR winds by starting the acceleration in the deep layers well below of what an observer would describe as the photosphere goes back to Kato & Iben (1992). While their model had a continuum-driven wind with an artificially enhanced opacity, the release of the OPAL opacities then let Pistinner & Eichler (1995) to follow up on this concept without the principal need of an artificial opacity enhancement. GH2005 for the first time developed a model with a consistent flux-weighted mean opacity including the Fe IX–XVI ions from Opacity Project data (e.g. Mendoza et al. 2001). They demonstrated, that the launch of the wind in the deep layers implies a smaller radius than commonly assumed when analysing WR stars with models using a prescribed β -law (cf. the results for WR 111 in Sander et al. 2012, 2019). As a consequence, the population of Fe IX–XVI, the so-called M-shell ions, is significantly enhanced, providing sufficient acceleration for launching a WR wind. The corresponding opacity is essentially forming the ‘(hot) iron bump’ in the OPAL tables by Iglesias & Rogers (1996).

The empirical constraint of WR radii is cumbersome as WR spectra tend to form solely in the wind. This has led to discrepancies between empirical results and hydrostatic radii predicted by stellar evolution models. WR radii are an important important constrain in massive star evolution e.g. to determine the progenitor systems of double black hole binaries (e.g. Marchant et al. 2016). In this work, we investigate compact WR atmosphere models, motivated by the result from GH2005 hinting that the larger radii in em-

pirical models might just be a consequence of their simplified (i.e. β -law) treatment of the density and velocity stratification. While hydrostatic stellar structure calculations (e.g. Gräfener et al. 2012; McClelland & Eldridge 2016) yield so-called ‘inflated’ hydrostatic radii for WR stars, recent hydrodynamic structure calculations by Grassitelli et al. (2018) support and generalize the picture of He stars with a compact subsonic structure and an extended pseudo-photosphere at large radii. Such models demonstrate that optically thick winds compatible with the empirical \dot{M} for WNE stars can be launched by the hot iron bump, consistent with the results from the hydrodynamic atmosphere model for WR 111 by GH2005.

In the last decade it has further become clear that the most massive stars in the Universe are not O-type stars, but WR stars with H, termed WNh stars (Hamann et al. 2006; Martins et al. 2008; Liermann et al. 2010) with up to 200–300 solar masses (Crowther et al. 2010). These very massive stars (VMS; Vink et al. 2015) are predicted to have strong, Γ_e -dependent \dot{M} (Vink 2006; Gräfener & Hamann 2008), which is confirmed by empirical results (Gräfener et al. 2011; Bestenlehner et al. 2014). Γ_e denoted the ratio of acceleration due to Thomson scattering and gravity, i.e. $\Gamma_e \propto q_{\text{ion}} \cdot L/M$ (cf. e.g. Eq. 22 in Sander et al. 2015). While for canonical O-type stars Vink et al. (2011) predicted a relatively shallow Γ_e -dependence in relatively good agreement with CAK, for optically denser winds where the wind efficiency parameter

$$\eta := \frac{\dot{M}v_{\infty}}{L/c} \quad (1)$$

crosses unity (Vink & Gräfener 2012), \dot{M} shows a much steeper Γ_e -dependence, resulting in a ‘kink’ in the derived $\dot{M}(\Gamma_e)$ -relation, seemingly in disagreement with the CAK theory. Given that VMS/WNh winds are only marginally optically thick, while cWR winds are usually very optically thick, we will explore a regime beyond the applicability of CAK, where a new generation of hydrodynamically consistent atmospheres becomes a necessity for a profound understanding of WR and He star winds in general.

The paper is organized as follows: after we introduce the stellar atmosphere models in Sect. 2, the following Sect. 3 comprises a detailed discussion of the radiative acceleration in WR atmospheres. In Sect. 4, we then discuss the sets of calculated models and their implication for wind driving and mass-loss of cWR stars. The main insights from the paper are comprised in the concluding Sect. 5. In the appendix, we furthermore demonstrate the breakdown of a CAK force multiplier approach for cWR stars (Sect. A) due the complex, non-monotonic opacity structure, and discuss the problem of finding an analytic description for the radiative acceleration (Sect. B).

2 STELLAR ATMOSPHERE MODELS

For our study we use the PoWR model atmosphere code (e.g. Gräfener et al. 2002; Hamann & Gräfener 2003; Sander et al. 2015) with the option to solve to hydrodynamically consistent stratifications introduced in Sander et al. (2017). The models assume a spherically symmetric star with an expanding, but stationary outflow. To properly account for the non-LTE conditions of hot star atmospheres, the population numbers for all levels (cf. Table C2) are calculated by solving the high-dimensional system of statistical equilibrium equations. The radiative transfer is treated in the co-moving frame (CMF) to avoid any major simplifications (cf. e.g. Mihalas et al. 1975). Together with the calculation of the temperature stratification, the solution of the statistical equations and the

radiative transfer are performed iteratively until a consistent model for the full atmosphere is obtained. Hydrodynamic stratification updates, meaning new calculations of the velocity and density structure from the hydrodynamic equation of motion, are performed and applied every time the corrections to the populations numbers have dropped below a certain limit and the flux is reasonably well conserved (usually on the order of a few percent). Once the overall iteration cycle including the stratification updates is converged, the emergent spectrum of the star is calculated from the formal integral in the observer's frame. A more detailed description of the concepts of these 'next-generation' PoWR models is given in [Sander et al. \(2017\)](#).

The inner boundary of our models, where we assume the diffusion approximation to be valid, is defined by the stellar radius R_* , which we define at a Rosseland continuum optical depth of $\tau_{\text{Ross,cont}} = 20$. This quantity is conserved during all stratification updates, thus ensuring our input parameters T_* and L , connected by the Stefan-Boltzmann law

$$L = 4\pi R_*^2 \sigma_{\text{SB}} T_*^4, \quad (2)$$

remain consistent. L denotes the luminosity of the star, while T_* is the effective temperature corresponding to R_* , meaning $T_* := T_{\text{eff}}(R_*) = T_{\text{eff}}(\tau_{\text{Ross,cont}} = 20)$. As this is deep in the optically thick regime, this effective temperature is not identical to the electron temperature T_e . In fact, $T_e(R_*)$ is typically on the order of $\approx 2 \dots 2.5 T_*$ for classical Wolf-Rayet stars. The considerable scatter is a consequence of $T_e(R_*)$ depending on the total optical depth including lines τ_{Ross} , i.e.

$$T_e(R_*) \approx T_* \sqrt[4]{\frac{3}{4} \tau_{\text{Ross}}(R_*) + \frac{1}{2}}, \quad (3)$$

instead of just $\tau_{\text{Ross,cont}}$. Choosing a fixed $\tau_{\text{Ross,cont}}$ as a boundary value is numerically favourable, but as the ratio between $\tau_{\text{Ross}}(R_*)$ and $\tau_{\text{Ross,cont}}(R_*)$ varies for different model parameters, this comes at the cost of the described scatter in $T_e(R_*)$.

Another common definition for the effective temperature of a star is to refer to the radius where the Rosseland optical depth is equal to $2/3$. We define this value as $T_{2/3} = T_{\text{eff}}(\tau_{\text{Ross}} = 2/3)$ in our work and will discuss the role of its corresponding radius $R_{2/3}$ later in Sect. 3. Further input parameters for each PoWR model are the stellar mass M_* , the mass-loss rate \dot{M} , the clumping stratification $D(r)$, and an initial approximation for the velocity $v(r)$. The density structure is implied via the equation of continuity

$$\dot{M} = 4\pi r^2 \rho(r) v(r). \quad (4)$$

In all models presented in this work, $v(r)$ is iteratively adjusted, while the mass-loss rate \dot{M} can either be updated as well or kept fixed. In the latter case, another fundamental stellar parameter of course has to be changed instead. For the stratification update in our code we allow to either

- keeping L and M_* fixed to determine the consistent \dot{M} ,
- fixing L and \dot{M} to deduce the consistent M_* , or
- keeping instead M_* and \dot{M} fixed to obtain the consistent L .

The general numerical implementation is very similar that described in [Sander et al. \(2017\)](#), but the flexibility to switch between these different methods allows us to use in each case the correction mechanism that is of interest for our particular study and numerically most efficient. As the CMF radiative transfer is usually the bottleneck in terms of calculation time, choosing the method that leads to corrections least affecting the radiative transfer is a significant help to keep the computational effort manageable. It is

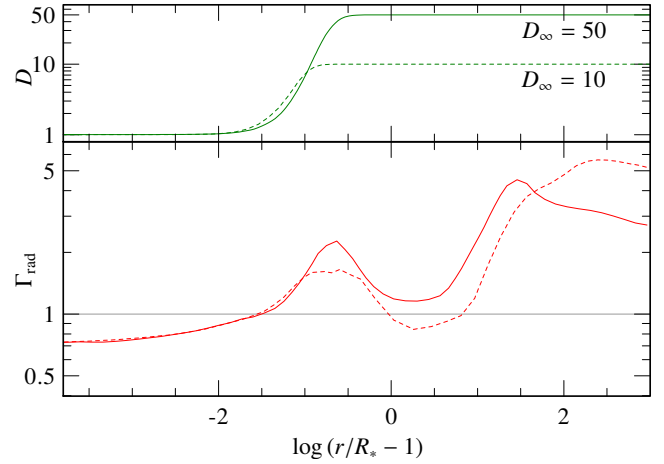


Figure 1. Comparison of the radiative acceleration normalized to gravity ($\Gamma_{\text{rad}} = a_{\text{rad}}/g$, lower panel) and the clumping stratification (upper panel) for WN models with $D_\infty = 10$ (dashed lines) and $D_\infty = 50$ (solid lines).

important to keep in mind that this choice of what is a fixed input and what is updated is purely for computational reasons. Test calculations were performed to ensure that the different methods do not lead to conflicting results. Hence, the finally obtained sets of L , M , and \dot{M} are consistent between the different methods and can always be read as the mass-loss rate \dot{M} following from a set of given stellar parameters L and M , regardless of the actual computational method.

We choose a depth-dependent clumping stratification with a maximum clumping factor of $D_\infty = 50$. With a void interclump medium, this corresponds to a volume filling factor $f_V = D^{-1} = 0.02$. While this value is in the range of what has been used for several OB star analyses (e.g. [Bouret et al. 2012](#); [Mahy et al. 2015](#)), we are aware that it is considered to be more towards the drastic end of what is actually considered to be reasonable, while $D \approx 10$ or $f_V = 0.1$ is more commonly applied and usually more consistent with what is inferred from electron scattering wings. However, the two main reasons to keep this value are to be consistent with the only previously existing consistent early-type WR model by [GH2005](#) and to particularly avoid $\Gamma_{\text{rad}} < 1$ in the wind which would lead to a non-monotonic velocity profile, which then would need to be modified in order to work within our CMF radiative transfer framework. Since we are using a depth-dependent approach for $D(r)$, the actual effect on the derived \dot{M} for a given set of T_* , L , and M_* is really small (≈ 0.03 dex) between $D_\infty = 10$ and $D_\infty = 50$ as long as the same recipe for $D(r)$ is used. The reason for this is illustrated in Fig. 1, where one can see that the radiative acceleration equals gravity (i.e. $\Gamma_{\text{rad}} = 1$) already in a region where $D(r)$ has not yet reached its maximum value (and Γ_{rad} also drops back below 1 for the $D_\infty = 10$ -model). Instead the – empirically highly uncertain – onset of clumping can play an important role. However, since this would add at least one more dimension, we limit this work to models using the depth-dependent descriptions via τ and v explained in [Sander et al. \(2017\)](#) with $\tau_{\text{cl}} = 10$ or $v_{\text{cl}} = 100 \text{ km s}^{-1}$ and point out the need for a future, more in-depth study of the imprint of the clumping stratification on the driving of WR winds. Our choice of $D_\infty = 50$ affects of course the derived terminal velocities v_∞ . Test calculations in regimes where solutions for both $D_\infty = 50$ and $D_\infty = 10$ could be obtained, e.g. for very dense winds

with $\log \dot{M} \approx -4.4$, reveal that v_∞ is about 30% larger for $D_\infty = 50$ compared to a similar calculation with $D_\infty = 10$.

As introduced in Sander et al. (2015) and discussed in Sander et al. (2017), we can write the hydrodynamic equation of motion as

$$v \left(1 - \frac{a^2}{v^2} \right) \frac{dv}{dr} = a_{\text{rad}} - g + 2 \frac{a^2}{r} - \frac{da^2}{dr} \quad (5)$$

$$= \frac{GM}{r^2} (\Gamma_{\text{rad}} - 1) + 2 \frac{a^2}{r} - \frac{da^2}{dr} \quad (6)$$

with a_{rad} denoting the total radiative acceleration which we will discuss in Sect. 3 in more detail. The quantity $a(r)$ denotes the isothermal sound speed a_s corrected for a micro-turbulence term, i.e.

$$a^2(r) := \frac{k_B T(r)}{\mu(r) m_H} + \frac{1}{2} v_{\text{mic}}^2 \equiv a_s^2 + \frac{1}{2} v_{\text{mic}}^2 \quad (7)$$

with v_{mic} assumed to have a constant value of 30 km s^{-1} in this work. While such a constant micro-turbulence likely does not reflect the true situation in a WR atmosphere, the potential parameters which can be varied in a model atmosphere are manifold. Thus, we decided to focus on the more fundamental parameters in this work, leaving the finer contributions such as v_{mic} or a detailed discussion of the clumping stratification $D(r)$ to be discussed in a future work.

The hydrodynamic equation of motion in the form of Eq. (5) or Eq. (6) has a critical point at $R_{\text{crit}} := R(v = a)$, that is the radius where the wind speed v is equal to the turbulence-adjusted sound speed. Due to the parametrization of a_{rad} as a function of radius, this critical point is not identical to the CAK critical point, which would be located further out. Since we include a micro-turbulence term in $a(r)$, we refrain from calling it the ‘sonic point’ to avoid any confusion with the radius where $v = a_s$, which is slightly further in due to $v_{\text{mic}} > 0$. A more detailed study of the influence of v_{mic} is beyond the scope of the present paper, but one has to be aware that the origin of turbulence is commonly attributed to sub-surface convection zones (e.g. Cantiello et al. 2009; Grassitelli et al. 2015; Jiang et al. 2015), which would likely be incompatible with a wind launching mechanism at the hot iron bump (e.g. Ro & Matzner 2016). However, the value of 30 km s^{-1} chosen in this work has only a very limited influence on the location of the critical point. We illustrate this in Fig. 2, highlighting both R_{sonic} and R_{crit} for a typical WNE model at Z_\odot where both radii differ by only $0.002 R_*$. Thus, even the complete absence of turbulence would lead to only a small change of our results derived in this work.

3 THE RADIATIVE ACCELERATION

The strength, but also the complexity of our locally consistent hydrodynamical approach is rooted in the detailed treatment of the radiative transfer, which is performed in the CMF to keep the opacities and emissivities isotropic despite the expansion. From the CMF radiative transfer we also obtain the radiative acceleration which we can write in 1D as

$$a_{\text{rad}}(r) = \frac{4\pi}{c} \frac{1}{\rho(r)} \int_0^\infty \kappa_\nu(r) H_\nu(r) d\nu \quad (8)$$

$$= \frac{4\pi}{c} \int_0^\infty \kappa_\nu(r) H_\nu(r) d\nu. \quad (9)$$

By not assuming any explicit analytical expression for a_{rad} , we implicitly account for various effects such as line overlaps and multiple scattering. The two flavors of Eq. (8) depend on whether the

opacity is written in the form of an absorption coefficient κ_ν that has the units of an inverse length (i.e. cm^{-1}), or as a mass attenuation coefficient κ_ν in $\text{cm}^2 \text{ g}^{-1}$ with $\kappa_\nu(r) = \rho(r) \kappa_{\nu}(r)$. As mentioned in Sander et al. (2017), this opacity includes all line and continuum opacities, i.e. bound-bound, bound-free, and free-free transitions as well as Thomson electron scattering. Especially the so-called ‘true continuum’ of bound-free and free-free transitions, which is usually negligible for OB star winds, can become important for WR star winds at some depths and thus cannot be neglected a priori.

Using a_{rad} in the form of Eq. (9) allows to eliminate the explicit dependence of the density. Replacing the Eddington flux H_ν with $F_\nu = 4\pi H_\nu$ and introducing the flux-weighted mean opacity

$$\kappa_F(r) = \frac{1}{F(r)} \int_0^\infty \kappa_\nu(r) F_\nu(r) d\nu \quad (10)$$

with $F = \int F_\nu d\nu$ it is often written as

$$a_{\text{rad}}(r) = \frac{1}{c} \kappa_F(r) F(r) = \frac{\kappa_F(r) L}{4\pi r^2 c}. \quad (11)$$

In the last equation, we used $L(r) = 4\pi r^2 F(r)$ to express the integrated flux F by the stellar luminosity L . For very dense winds, L is not exactly constant as the energy removed for driving the wind could in theory become large enough to reduce the observed luminosity. However, even in our Wolf-Rayet calculations this is a minor effect. In this work, we yield $\Delta \log L/L_\odot < 0.05$ for the most extreme (i.e. high \dot{M} and high Z) considered cases.

Instead of a_{rad} , it is often more favourable to discuss the ratio

$$\Gamma_{\text{rad}}(r) := \frac{a_{\text{rad}}(r)}{g(r)} = \frac{\kappa_F(r) L}{4\pi c G M}. \quad (12)$$

Since the mass of the stellar atmosphere compared to the total mass is negligible and also L is approximately constant, all radial dependency of Γ_{rad} is due to the flux-weighted mean opacity κ_F . The quantity κ_F should not be mixed up with the Rosseland opacity

$$\kappa_{\text{Ross}}^{-1}(r) := \frac{\int_0^\infty \kappa_\nu^{-1}(r) \frac{\partial B_\nu}{\partial T} d\nu}{\int_0^\infty \frac{\partial B_\nu}{\partial T} d\nu} \quad (13)$$

that is for example used in stellar structure calculations or wind driving studies based on the grey OPAL opacity tables (e.g. Nugis & Lamers 2002; Ro & Matzner 2016; Gräfener et al. 2017; Sanyal et al. 2017; Grassitelli et al. 2018; Ro 2019). In the deeper layers of the atmosphere where the diffusion approximation is valid, $\kappa_F \approx \kappa_{\text{Ross}}$ holds as illustrated in Fig. 2, but the difference between the two quantities becomes considerable around and above the critical point with the two quantities being off by more than an order of magnitude in the outer wind. Thus, the construction of a consistent wind stratification cannot be achieved without the detailed calculation of κ_F , as only this quantity gives a proper handle on the radiative acceleration and the driving of a stellar wind.

In analogy to the Rosseland optical depth, we can define the flux-weighted optical depth

$$\tau_F(r) := \int_r^\infty \kappa_F(r') \rho(r') dr' \quad (14)$$

which can serve as an optical depth scale directly reflecting the wind driving situation. A comparison with the more common τ_{Ross} for a typical hydrogen-free WN model at Z_\odot is depicted in Fig. 3. While in the innermost region both scales approach the same total value, their difference is quite remarkable in the outer layers. In particular the region where the wind is optically thick ($\tau_F > 2/3$) is

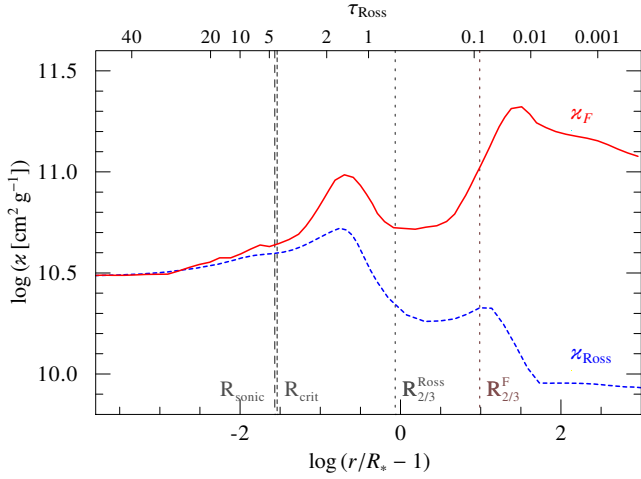


Figure 2. Comparison of the flux-weighted mean opacity (red, solid) to the Rosseland mean opacity (blue, dashed) in an atmosphere model for a hydrogen-free WN star (see Table 1 for parameters) at solar metallicity.

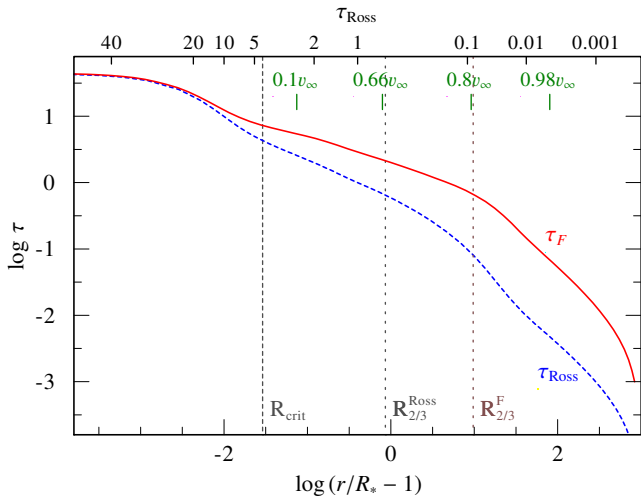


Figure 3. Comparison of the flux-weighted optical depth (red, solid) to the Rosseland optical depth (blue, dashed) in an atmosphere model for a hydrogen-free WN star (see Table 1 for parameters) at solar metallicity.

by an order of magnitude larger than what one would infer from the Rosseland scale. At this distance of $\approx 11 R_*$, the wind has already reached more than 80% of its terminal velocity. To distinguish the corresponding radius for the two different optical depth scales we denote them as $R_{2/3}^{\text{Ross}}$ and $R_{2/3}^{\text{F}}$, respectively. Wherever a quantity is labeled only $R_{2/3}$, it has the meaning of $R_{2/3}^{\text{Ross}}$.

For our hydrodynamically consistent models, we demand that the sum of radiation (following from κ_F , cf. Eq. 11) and gas pressure (including turbulence) to be equal to the sum of gravity and inertia throughout the stellar atmosphere. This is illustrated in Fig. 4 where we show the acceleration balance for an example WNE model. The figure also shows that the contributions to a_{rad} from free electron (Thomson) scattering and the total continuum which includes the opacities from bound-free and free-free transitions on top of the Thomson contribution. Although numerically crucial to get the proper critical point, the actual contribution of the gas and turbu-

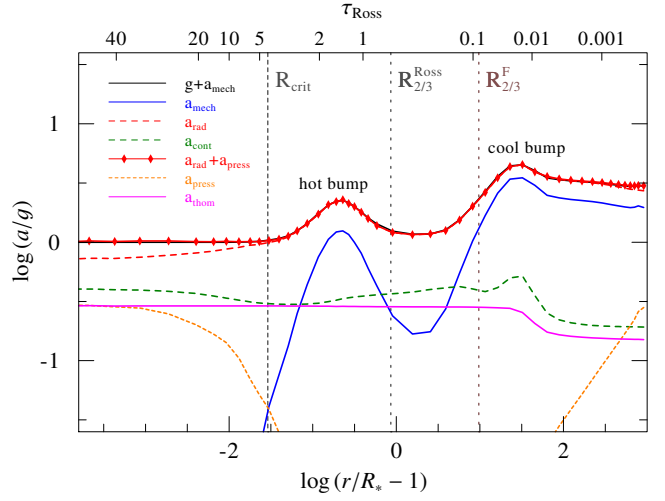


Figure 4. Acceleration stratification for a hydrodynamically consistent WNE model with $Z = Z_{\odot}$ (see Table 1 for parameters): the sum of gravity and inertia (black solid line) matches the total wind acceleration (red diamond line). The contributions to these two terms are indicated by different line styles and colors as indicated in the plot. The so-called hot and cool bump stemming from the line acceleration contribution are also labelled. The particular ions contributing ions to the bumps are shown in Fig. 13.

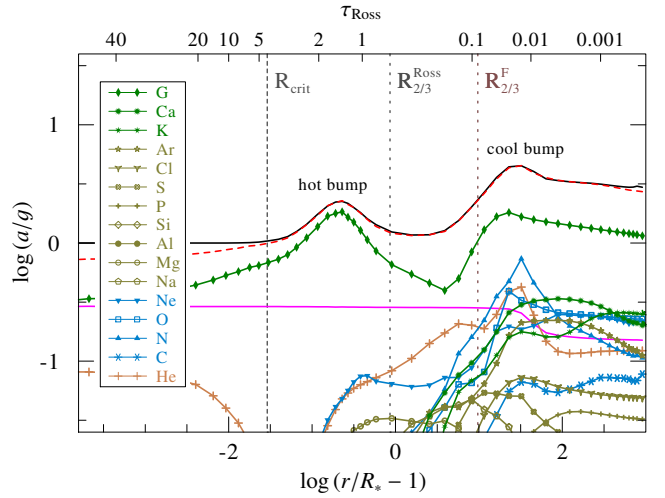


Figure 5. Contributions to the radiative acceleration by different elements for the same models as depicted in Fig. 4: The sum of gravity and inertia (black solid line) and the total radiative acceleration (red dashed line) are added for comparison, as well as the contribution due to free electron scattering (purple solid line). The element ‘G’ stands for a generic element representing the whole iron group (see Gräfener et al. 2002).

lent pressure gradients is small and becomes important only closer to the boundaries: in the deeper subsonic layers, where the contributions from the line acceleration get smaller and smaller, it raises to about 30%. In the far outer wind, its relative contribution grows to the fact that there is a $1/r$ -term in a_{press} compared to the $1/r^2$ -terms of the other forces which decline more rapidly.

From Fig. 4, we can infer that the main contribution to a_{rad} is due to the line acceleration. The two ‘bumps’, already present in the κ_F -curve in Fig. 2, are termed the ‘hot’ and ‘cool’ bump and can be understood when breaking a_{rad} down into the contributions of the

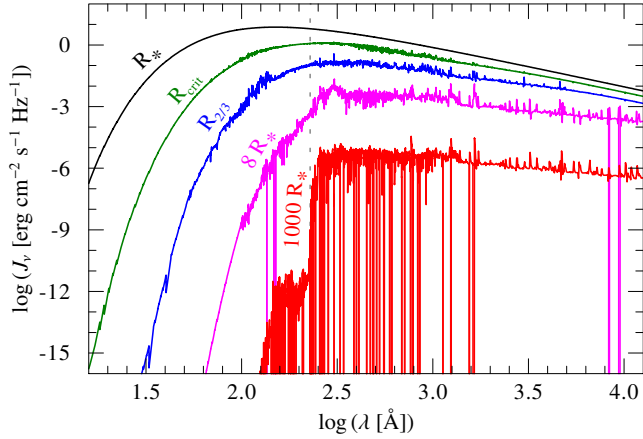


Figure 6. The radiation field $J_\nu(r, \lambda)$ in the comoving frame at different distances r from the inner boundary R_* , corresponding to a Rosseland continuum optical depth of $\tau_{\text{Ross,cont}} = 20$. Note that the curves in this figure are plotted on the coarse frequency grid used in the calculation of the radiative rates, while the radiative transfer itself is performed on a finer grid. For computational and memory reasons, the fine-grid results are not stored permanently. The dashed vertical line denotes the He II ionization edge. (WNE model at Z_\odot , see Table 1 for a complete set of parameters.)

different elements (Fig. 5). It is evident, that both bumps are mainly caused by iron group opacities (treated as the generic element G) although there are additional significant contributions to a_{rad} , especially in the outer wind. The ‘cool’ bump is further increased by N, O, and He contributions, with the latter stemming from bound-free opacities. In models with dense winds like our WNE example here, He III is no longer the leading ionization stage, but instead most of the He recombines into He II. As a consequence of less available free electrons, the Thomson contribution decreases.

In addition to the iron group elements, several other elements contribute to the acceleration in the outer wind. It is noteworthy that this is not limited to the CNO elements, but instead the more heavy and electron-rich Ca, K, and Ar provide important contributions here. Moreover, Ne is on the same order as oxygen, while the influence of C is much lower due to the depleted abundance in WN stars. Elements such as Si, P, or S, which are important to consider for O or B stars (e.g. Vink et al. 1999; Noebauer & Sim 2015; Sander et al. 2017, 2018), provide only minor or even negligible contributions to the wind driving in a WNE. A full list of all considered elements and ions is listed in the appendix Table C2.

In Fig. 6, the angle-integrated intensity J_ν is shown as a function of wavelength λ at different distances from R_* . At the inner boundary of our stellar atmosphere we are in an optically very thick regime ($\tau_{\text{Ross,cont}} = 20$, $\tau_{\text{Ross}} \approx 44$), where we can safely assume the diffusion approximation to be valid. Thus, the resulting J_ν is an almost perfect blackbody. This changes outwards as depicted in Fig. 6, but the departures from a blackbody are not large as long as we remain in the optically thick regime, which includes our critical point at $\tau_{\text{Ross}} \approx 4$. In the wind however, the shape of J_ν is significantly altered, especially in the outer wind where most of the He II ionizing photons are absorbed. While not obvious from Fig. 6, the photons are re-emitted at longer wavelengths, leading to an emergent flux $\propto \lambda^{-2.9}$ as illustrated in Fig. 7, considerably flatter than the λ^{-4} -slope one would infer from the Rayleigh-Jeans part of a blackbody. Defining an effective temperature for a WR star is not straight-forward due to the fact that for these dense winds the

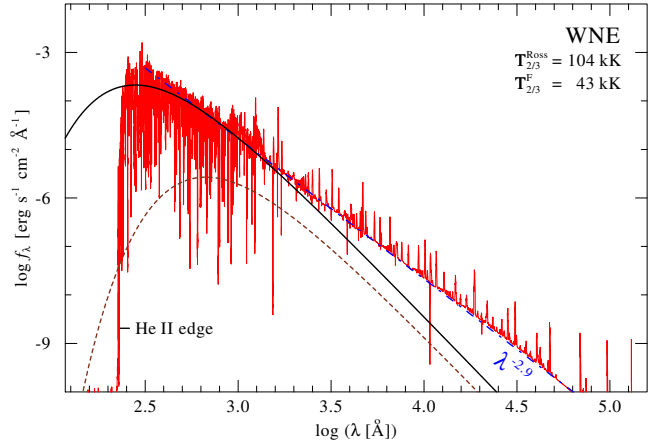


Figure 7. Emergent spectral energy distribution (red) of a WNE (same as in Fig. 6) compared to black bodies with effective temperatures obtained from $\tau_{\text{Ross}} = 2/3$ (black) and $\tau_F = 2/3$ (maroon, dashed). The blue dot-dashed line represents the slope of the spectrum redwards of the flux peak in the UV. The EUV flux drop corresponds to the He II ionization edge.

whole spectrum is formed in the wind. In Fig. 7, we use the effective temperature corresponding to $R(\tau_{\text{Ross}} = 2/3)$ and $R(\tau_F = 2/3)$ for comparison. While the flux-weighted optical depth τ_F is important in terms of wind driving, $T_{\text{eff}}(\tau_F = 2/3)$ does not provide any useful representation. Instead, the Rosseland optical depth here represents where the continuum part of the spectrum is formed and we thus define $T_{2/3} := T_{\text{eff}}(\tau_{\text{Ross}} = 2/3)$. The corresponding blackbody touches the actual slope of the emergent spectrum in the UV, but cannot reproduce the other main features. It is clear that a blackbody is not a good representation of the emergent flux of a WR star. Even when adding a cutoff at the He II ionization edge, any blackbody representation would significantly underestimate the flux at longer wavelengths. Due to the different slope, the amount of underestimation is wavelength-dependent, but easily surpasses an order of magnitude already in the near-IR, getting larger ever after. This effect is more pronounced for denser winds with the slope going back to Rayleigh-Jeans in the thin-wind limit. Even then, for a star with $T_* \approx 140$ kK the emergent flux at short (e.g. EUV) wavelengths can still deviate from a blackbody by an order of magnitude.

4 RESULTS

In this work we calculate different series of models, anchored by the prototypical model for WR 111 by GH2005. We limit our study to models with $T_* = 141$ kK, reflecting early-type, He-burning stars with compact R_* (as recently also motivated by Grassitelli et al. 2018). Corresponding to the WC model with $\log \dot{M} = -5.15$, we calculated a WNE model with the same \dot{M} . These were then used as anchors for different model sets. In the first set, we calculated a series of models with fixed \dot{M} and flexible Γ_e or, respectively, L/M_* -ratio, where we vary the metallicity Z ranging from 10 times solar down to 10^{-5} times solar. In the second and third series, we fix Z to $1 Z_\odot$ and $0.1 Z_\odot$, while exploring the $\dot{M}(\Gamma_e)$ domain.

A detailed set of input and output parameters for the anchoring WNE and WC models at Z_\odot with $\log \dot{M} = -5.15$ is given in Table 1. (The third model with $\log \dot{M} = -6.1$ refers to the WC model with a thin wind and is shown for comparison. The different implications in regards to driving for optically thin solutions are discussed fur-

ther below and, with specific reference to this model, in Sect. A of the appendix.) The chemical composition given in Table 1 is identical for all other models at Z_{\odot} in this work. Throughout the rest of this paper, we refer to the metallicity Z in the sense of non self-enriched elements. Thus for WC models, this excludes C and O, which are kept at $X_{\text{C}} = 0.6$ and $X_{\text{O}} = 0.05$ for all Z unless otherwise noted. In the WNE models, the CNO elements are mixed due to the bottleneck in the CNO cycle, leading to a nitrogen enhancement. These mixed abundances are then scaled for WN models at different Z .

T_* , v_{mic} and D_{∞} are kept fixed throughout this work. The choice of $T_* = 141$ kK implies that our solutions will likely not be applicable for late-type WR stars. For these types, the discrepancy between the empirically deduced values for T_* and the effective temperatures inferred from hydrostatic stellar evolution calculations are largest. Via Eq. (2), this temperature discrepancy can also be viewed as a radius discrepancy and has been termed the ‘WR radius problem’ (e.g. Grassitelli et al. 2018). The prototypical study by GH2005 has shown that for the WC5 star WR 111 this discrepancy could be removed by using a hydrodynamically consistent stratification, where T_* changed from 85 kK to 140 kK and R_* is reduced from $\approx 2.5 R_{\odot}$ to $0.9 R_{\odot}$, in line with a star essentially sitting on the He zero age main sequence (He-ZAMS). In light of this result, we calculate such compact, hydrodynamically consistent models in this work and leave a broader study of the T_* -domain for future work.

Comparing our anchoring models reveals that when we force both models to have the same \dot{M} , the WNE star has a higher stellar mass. In turn, this implies a WNE star with the same M_* (and L) as a WC star can drive a wind with a higher \dot{M} . While the higher C and O abundances in a WC star do not lead to an increase of its mass-loss rate compared to a WNE star as their ionization stages are too high at the high electron temperatures around R_{crit} to provide substantial line driving, they provide additional opacity in the wind, leading to higher terminal velocities. This also holds when we fix M_* : In a test case with $M_* = 11 M_{\odot}$ and $\log L/L_{\odot} = 5.45$, we obtain $\log \dot{M} = -4.8$ and $v_{\infty} = 2052 \text{ km s}^{-1}$ for the WNE, while we get $\log \dot{M} = -4.9$ and $v_{\infty} = 2159 \text{ km s}^{-1}$ for the WC star. While the difference in v_{∞} is a direct result of enhanced line-driving, the inverse difference in \dot{M} is not. As Table 1 illustrates, the WNE has a higher value for the ionization parameter q_{ion} and thus a higher $\Gamma_{\text{e}} \propto q_{\text{ion}} \cdot L/M$ (cf. Eq. 22 in Sander et al. 2015). For fixed L/M , it is therefore only the larger He mass fraction in the WNE making the difference. More He instead of C and O leads to more free electrons compared the WC stars, thus increasing the Thomson contribution and therefore the mass-loss rate. The only elements that can provide substantial line opacities directly affecting \dot{M} are those with complex electron structures such as iron, while others only have an indirect effect via their contribution to the free electron budget.

Comparing the WC parameters in Table 1 to the results from GH2005, we see only minor discrepancies. This is a bit surprising given the fact that GH2005 used way fewer elements and a much larger value of $v_{\text{Dop}} = 250 \text{ km s}^{-1}$ in the CMF calculations. While necessary at that time to speed up the calculations, this also leads to an additional broadening of the iron-line cross sections compared to our more standard estimate of $v_{\text{Dop}} = 100 \text{ km s}^{-1}$. We thus also calculated additional models with both values of v_{Dop} using their original chemical composition and clumping stratification, revealing that the various differences between their and our approach partly cancel each other, leading to the good agreement. The calculations further revealed that the terminal velocity v_{∞} in these kind of models is very sensitive to all kinds of changes, including the

Table 1. Hydrodynamically consistent WNE and WC models with Z_{\odot}

	WNE	WC	WC (thin)
T_* [kK]		141	
R_* [R_{\odot}]		0.9	
$\log(L [L_{\odot}])$		5.45	
$\log(\dot{M} [M_{\odot} \text{ yr}^{-1}])$	-5.15	-5.15	-6.1
$v_{\text{mic}} [\text{km s}^{-1}]$		30	
D_{∞}		50	
X_{H}		–	
X_{He}	0.9787	0.6182	0.6182
X_{C}	$4.0 \cdot 10^{-4}$	0.6	0.6
X_{N}	0.015	–	–
X_{O}	$1.0 \cdot 10^{-3}$	0.05	0.05
X_{Ne}		$1.3 \cdot 10^{-3}$	
X_{Na}		$2.7 \cdot 10^{-6}$	
X_{Mg}		$6.9 \cdot 10^{-4}$	
X_{Al}		$5.3 \cdot 10^{-5}$	
X_{Si}		$8.0 \cdot 10^{-4}$	
X_{P}		$5.8 \cdot 10^{-6}$	
X_{S}		$3.1 \cdot 10^{-4}$	
X_{Cl}		$8.2 \cdot 10^{-6}$	
X_{Ar}		$7.3 \cdot 10^{-5}$	
X_{K}		$3.1 \cdot 10^{-6}$	
X_{Ca}		$6.1 \cdot 10^{-5}$	
X_{Fe}		$1.6 \cdot 10^{-3}$	
<i>Results:</i>			
$v_{\infty} [\text{km s}^{-1}]$	1805	2132	4268
$M_* [M_{\odot}]$	14.9	13.9	19.4
$R_{\text{crit}} [R_*]$	1.03	1.03	1.04
$R_{2/3}^{\text{Ross}} [R_*]$	1.86	1.60	1.03
$R_{2/3}^{\text{F}} [R_*]$	10.7	7.74	1.19
$\tau_{\text{Ross}}(R_{\text{crit}})$	5.38	3.53	0.26
$T_{\text{e}}(R_{\text{crit}}) [\text{kK}]$	196	188	147
$T_{\text{eff}}(R_{\text{crit}}) [\text{kK}]$	139	139	139
$T_{2/3} [\text{kK}]$	95	112	140
$\langle \mathcal{A} \rangle$	4.06	7.17	7.17
q_{ion}	0.43	0.35	0.39
Γ_{e}	0.29	0.25	0.18
η	2.18	2.61	0.60

precise method of temperature correction. Thus we need to assume an uncertainty for v_{∞} of up to 10% in all our models presented in this work.

4.1 The driving role of Carbon and Oxygen in WC stars

For WC stars, the abundances of carbon and oxygen have an influence on the derived results. We investigate this with two series of models: One, where we fix L and \dot{M} to study the derived stellar masses, and a second where we fit L and M_* to investigate the influence on \dot{M} . The results are shown in Fig. 8, where we see that for both elements higher abundances are counter-productive in regards to wind launching. The same \dot{M} can be driven by a WC star with $X_{\text{C}} = 0.2$ that is about $1.5 M_{\odot}$ or 10% more massive than a WC star with $X_{\text{C}} = 0.6$. This means that for the same L and M_* , the WC star with the lower X_{C} would have a larger \dot{M} , in line with our result above that a WNE star with the same L and M as a WC star has the larger \dot{M} . Again, less C and O lead to a higher Thomson opacity. In actual stellar evolution this would of course go the other way round, as the amounts of carbon and oxygen are increasing with time. The resulting decrease of \dot{M} due to the increased mixing of He-burning

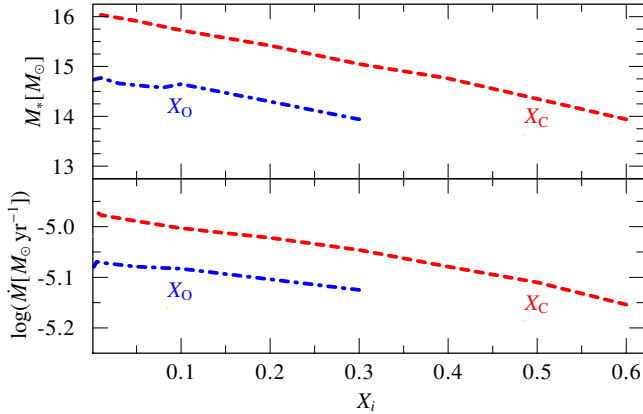


Figure 8. Upper panel: Stellar masses for hydrodynamically consistent WC star models with $\log L/L_\odot = 5.45$, $\log \dot{M} = -5.15 [M_\odot \text{yr}^{-1}]$, and different mass fraction of C (red, dashed, $X_O = 0.05$) and O (blue, dashed-dotted, $X_C = 0.4$). All other metals have solar abundances. Lower panel: Similar calculation, but now with fixed $M_* = 13.9$ and flexible \dot{M} .

products in the atmosphere however, is then also competing with the increase of \dot{M} due to the increase of $\Gamma_e \propto L/M$ during the life of a WC star resulting from the actual loss of mass itself.

Our second series depicted in the lower panel Fig. 8 confirms that – with the exception of $X_O < 0.005$, higher X_C and X_O decrease \dot{M} . The isolated dependence of a particular mass fraction on \dot{M} is exponential and a linear fit of $\log \dot{M}$ as a function of X_i yields

$$\log \dot{M} = -4.971(\pm 0.003) - 0.285(\pm 0.010)X_C \quad \text{and} \quad (15)$$

$$\log \dot{M} = -5.072(\pm 0.002) - 0.165(\pm 0.017)X_O, \quad (16)$$

revealing that a higher X_C seems to have about twice the impact of a higher X_O . Based on these findings and taking the empirically derived fractions for X_C and X_O , the uncertainty in \dot{M} of observed WC stars due to unsure abundances in C and O is about 0.2 dex.

4.2 Dependencies on luminosity and mass

In order reach a particular value for Γ_e or L/M_* in our calculations, we usually fix the luminosity L while varying the stellar mass M_* . This numerically favourable technique allows to calculate models for a good number of L/M_* values. As not all of these particular combinations of L and M_* will be realized in nature (see, e.g., Langer 1989), this of course prompts the question whether different combinations of L and M_* leading to the same Γ_e might affect the derived wind parameters such as \dot{M} , or only Γ_e matters here.

To investigate this, we calculated for two different mass-loss rates each a small series of WC and WN models with different luminosities. The derived values of Γ_e can be seen in the lower panel of Fig. 9. For the lower value of \dot{M} , Γ_e stays more or less constant, meaning that \dot{M} depends only on the ratio of L and M , but not the individual values themselves. For the larger \dot{M} however, we see a decrease of Γ_e with higher L . While a dependency on Γ_e is expected, the absence of a further L -dependence would be in contrast to relations for OB and WNh stars, which all include such a dependence (e.g. Vink et al. 2000; Gräfenor & Hamann 2008; Vink et al. 2011), meaning $\dot{M} = \dot{M}(\Gamma_e, L, T_*, X_i)$. For He-ZAMS stars, one could in principle eliminate either M or L from the recipe by using mass-luminosity relations (e.g. Langer 1989; Gräfenor et al. 2011), but as mentioned above this is not the intention of this paper which is purely based on atmosphere calculations.

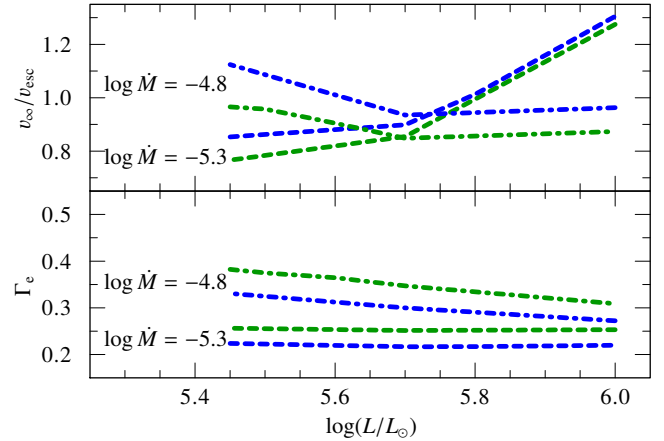


Figure 9. Eddington parameter $\Gamma_e(R_*)$ (lower panel) and v_∞/v_{esc} -ratio (upper panel) for consistent WN (green) and WC star models (blue) with different L and M , but identical \dot{M} .

A dependence of $\dot{M} = \dot{M}(\Gamma_e, T_*, X_i)$ would reduce the problem by one dimension and allow a simple scaling of the resulting \dot{M} to be e.g. easily used in stellar evolution calculations. The results for $\log \dot{M} = -4.8$ show that this is only approximately fulfilled. Fortunately, the remaining dependence on L does appear to be weak with e.g. $\log L/M_* \propto -0.155 \log L$ for our WC calculations.

In the upper panel of Fig. 9, we look at the outer wind layers, which seem to be more complex. Neither v_∞ , nor its ratio with the escape velocity $v_{\text{esc}} := \sqrt{2GM_*R_*^{-1}}$ remain constant for different L , but similar Γ_e . Including the factor $\sqrt{1 - \Gamma_e(R_*)}$ in the definition of v_{esc} changes the absolute values, but not the observed trends.

While the derived values for the terminal velocities have to be taken with care, the mass-loss rates appear to be more robust. In the following calculations, we will stick to $\log L/L_\odot = 5.45$. Our results can be approximately scaled to other luminosities (and masses) as long as L/M_* is kept constant. The small, but non-vanishing impact of L in our test models with higher \dot{M} means that such scaling introduces an uncertainty. Our $\dot{M}(\Gamma_e)$ -relations (cf. Sect. 4.4.2) thus need future follow-up calculations for different luminosity ranges.

4.3 Metallicity trends

A major uncertainty for our understanding of earlier generations of stars and galaxies is their mass-loss history. Line-driven mass loss requires a considerable abundance of elements with a sufficient number of lines covering the spectral energy distribution, especially in the UV and EUV. The iron group elements with in particular Fe itself are a key ingredient here. Thus, a lower abundance of Fe and other elements should considerably reduce the stellar mass loss.

4.3.1 Proximity to the Eddington Limit

To study how a certain amount of mass loss could be driven in different metallicity regimes, we calculate a series of models with constant \dot{M} , but different Z and consequently different L/M -ratios. An overview of the results from $10Z_\odot$ down to $10^{-5}Z_\odot$ is given in the Appendix Table C1 for WNE and WC stars respectively. The trend for $\dot{M}(Z)$ is also depicted in the upper panel of Fig. 10, where we see that WNE stars would need to get much closer to the Eddington limit at lower Z than WC stars due to the self-enriched

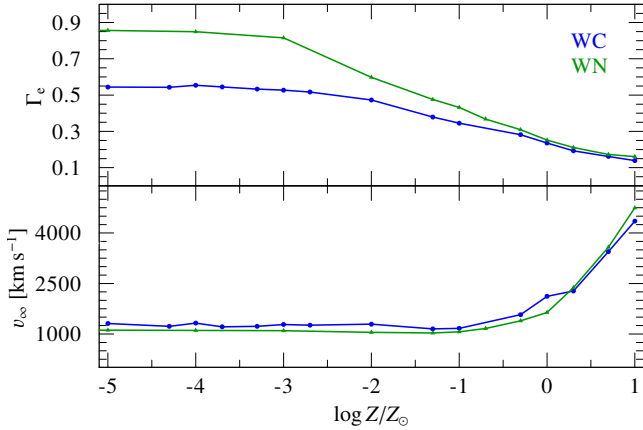


Figure 10. $\Gamma_e(Z)$ (upper panel) and $v_\infty(Z)$ (lower panel) for our WNE and WC sample (cf. Table C1) with the same luminosity and mass-loss rate

carbon abundance in WC stars. A closer look at the low- Z models reveals that this contribution is not only from spectral lines, but to a considerable part ($\approx 30..40\%$ depending on the layers) from the bound-free and free-free opacities of C III and C IV. For the WNE stars, where all non-He abundances scale with Z , the contribution from the true continuum is also significant at very low Z , but all of this can be attributed to He.

The true continuum is crucial for both, launching the wind and maintaining the acceleration. The obtained terminal velocities v_∞ would be considerably lower without taking these opacities into account. As they do not vanish at very low Z , the obtained values of v_∞ tend to stay essentially constant below $0.1Z_\odot$ as depicted in the lower panel of Fig. 10. In fact, there is a small increase of v_∞ with lower Z after a minimum is reached around $0.1Z_\odot$. As a direct consequence of the almost constant v_∞ and the fixed \dot{M} , the wind efficiency parameter η (cf. Eq. 1) does not change either at low Z as we vary our Γ_e by changing M_* while keeping L fixed.

In Fig. 11 we show the most important contributors for a WC star with a given mass-loss rate at different metallicities. Given an evolutionary scenario that could produce these objects, the self-enriched carbon surpasses the role of Fe for launching the wind at the critical point below $\log Z/Z_\odot \lesssim -2$ due to the contributions of the C IV continuum transitions. Vink & de Koter (2005) found that \dot{M} tends to settle for $\log Z/Z_\odot < -3$, which would agree with our finding that Fe continues to shrink in importance, but still plays a role until $\log Z/Z_\odot \approx -4$ where the line contributions from C IV and O VI are more important, although on an overall weak level of contribution. In the outer wind, a transition in the relative contributions happens already at higher Z than at the base of the wind: At $100R_*$, the importance of the C III continuum already surpasses iron below $\log Z/Z_\odot \lesssim 0.5$, i.e. below LMC metallicity.

For a WN model with $\log \dot{M} = -5.15$, we show the full radial dependency of the elements contributing to the radiative acceleration at three different Z in Fig. 12. Similar to what we saw in our discussion for the WC stars, Fe is the key element to launching the winds of classical WR stars at high metallicity. For lower Z this role weakens and the stars have to get closer to the Eddington limit to reach a similar mass loss. For $Z = 10^{-1}Z_\odot$, the role of free electron scattering is already a bit larger than the iron contribution. At very low Z , the line contributions for WN stars essentially disappear and winds at e.g. $10^{-3}Z_\odot$ are driven by continuum opacities. As long as the metallicity is not negligible, which tends to happen

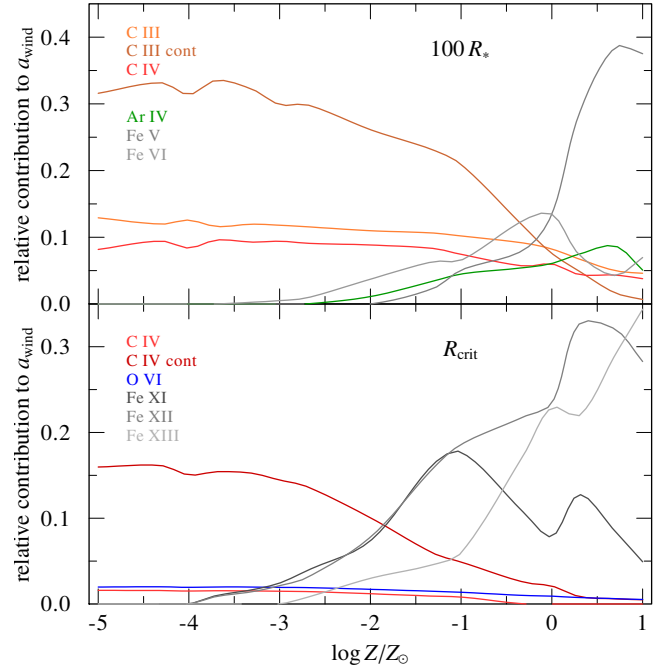


Figure 11. Lead line and true continuum contributions to the wind driving at R_{crit} (lower panel) and $100R_*$ (upper panel) for a WC star with $T_* = 141$ kK and $\log \dot{M} = -5.15$ at different Z

below $10^{-2}Z_\odot$, lower ionization stages are eventually reached in the outer wind and contributions from a variety of elements come into play. Major contributors here are N, O, Ne, Ar, and Ca with roughly equal impact despite their different abundances. Although the mass fractions of Ar and Ca are on the order of a few times 10^{-5} at Z_\odot , their transitions seem to fill up ‘gaps’ in frequency space, while elements of similar abundance like Al or Na do not.

As briefly mentioned in Sect. 3 and illustrated in Fig. 13, Si, P, and S do not provide a major contribution despite their abundance. On the contrary, the abundance of carbon is important, as it is depleted in favour of nitrogen due to the CNO cycle equilibrium. With X_C being about two orders of magnitude lower than X_N , its low contribution in WN winds is in sharp contrast to its significant role in WC winds. All of these results illustrate that the role an element plays for wind driving can neither be easily guessed from the abundance, nor from the general position in the periodic table of elements, but detailed consistent calculations of the non-LTE population and the radiative transfer are crucial.

4.3.2 Breakdown of mass loss at low Z

While we previously fixed \dot{M} and looked at the resulting L/M_* -ratio, we now consider the opposite approach and look at a WN and WC model with fixed L and M_* at different Z . The derived mass-loss rates in Fig. 14 reveal a dramatic decrease of \dot{M} with Z for both WR types. While the slope is modest between 0.5 and $2Z_\odot$ where \dot{M} varies by < 0.5 dex, the difference to the SMC regime is already an order of magnitude. At $0.1Z_\odot$, we get value of $\log \dot{M} \approx -8.4$, two orders of magnitude lower than for the SMC. Given the low metal abundance, such stars – if they exist – would have optically thin winds and provide a significant He II ionizing flux.

A steep dependence of $\dot{M}(Z)$ is known from theoretical modelling of massive OB star winds (e.g. Vink et al. 2001) and also

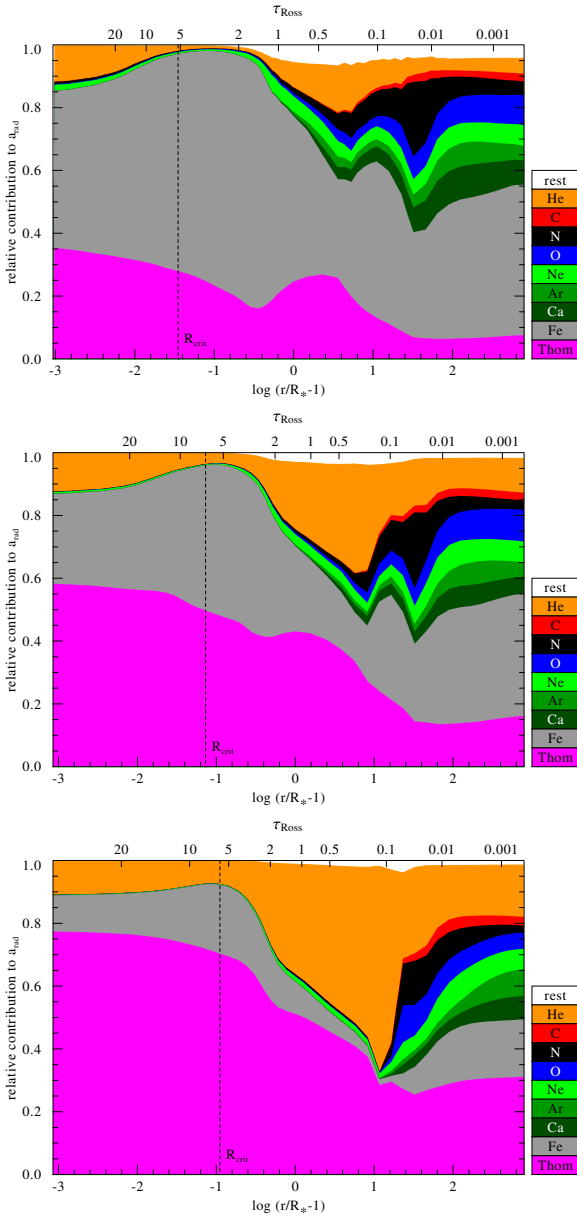


Figure 12. Relative contributions to a_{rad} for a WNE star at $Z = 1, 0.1,$ and $0.01 Z_{\odot}$ (top to bottom panels)

for the most massive stars which have WN-type spectra (Gräfener & Hamann 2008). Monte-Carlo calculations for late-type WN and WC stars by Vink & de Koter (2005) gave steep slopes of $\dot{M} \propto Z^{0.86}$ for WN and $\dot{M} \propto Z^{0.66}$ for WC stars in the regime between Z_{\odot} and $0.1 Z_{\odot}$. Empirically constrained results for WN stars by Hainich et al. (2015) yield an even steeper $\dot{M} \propto Z^{1.2}$. Our CMF-based models for early subtypes here point to an even steeper drop with lower Z that does not obey a simple power law. Calculations for He stars at $0.1 Z_{\odot}$ and below turn out to be challenging, giving the values at $0.1 Z_{\odot}$ a higher uncertainty. Nonetheless, the breakdown below Z_{SMC} is reproduced in various additional models that lead to sequences presented in Fig. 14.

Table 2. Parameters of the WR models calculated for the $\dot{M}(\Gamma_e)$ sequences ($T_* = 141 \text{ kK}$, $\log L/L_{\odot} = 5.45$)

$\log L/M$	$\Gamma_e(R_*)$	$\log \dot{M}$	v_{∞}	$T_{2/3}^{\text{Ross}}$	$T_e(R_{\text{crit}})$
<i>WN, solar abundances, CNO mixed</i>					
4.55	0.55	-4.39	2138	41	270
4.47	0.45	-4.59	2132	54	243
4.40	0.38	-4.79	2128	68	220
4.33	0.33	-5.00	2049	87	203
4.28	0.29	-5.16	2043	104	192
4.22	0.26	-5.29	2061	117	182
4.19	0.24	-5.50	1970	132	173
4.17	0.23	-5.70	2812	138	161
4.15	0.22	-5.89	3560	139	155
4.13	0.21	-6.09	4341	139	150
<i>WN, 0.1 solar abundances, CNO mixed</i>					
4.67	0.72	-4.39	1212	33	253
4.59	0.61	-4.59	1421	39	230
4.54	0.54	-4.79	1335	44	210
4.52	0.51	-4.89	1317	49	201
4.50	0.49	-5.00	1316	55	193
4.49	0.48	-5.09	1299	63	186
4.48	0.46	-5.20	1264	72	179
4.47	0.45	-5.29	1166	81	173
4.46	0.45	-5.39	1148	90	168
4.45	0.44	-5.50	1015	98	163
4.45	0.44	-5.59	1044	107	158
4.44	0.43	-5.79	1088	123	151
4.44	0.42	-6.00	1192	135	145
4.43	0.42	-6.20	1320	137	139
4.43	0.41	-6.39	1556	138	132
4.43	0.41	-6.59	1754	138	129
<i>WC, solar abundances, except for CNO</i>					
4.62	0.51	-4.39	2243	39	268
4.52	0.40	-4.59	2310	63	238
4.44	0.33	-4.79	2366	78	218
4.39	0.30	-4.89	2164	84	210
4.36	0.28	-5.00	2341	97	200
4.31	0.25	-5.15	2132	112	188
4.27	0.22	-5.29	2184	124	180
4.22	0.20	-5.50	2394	136	167
4.20	0.19	-5.70	2906	138	160
4.18	0.18	-5.89	3647	139	153
4.16	0.18	-6.09	4268	140	147
4.15	0.17	-6.29	4772	140	141
4.13	0.16	-6.50	5264	140	138
4.12	0.16	-6.70	6050	140	127
<i>WC, 0.1 solar abundances, except for CNO</i>					
4.71	0.63	-4.39	1724	41	250
4.67	0.57	-4.50	1689	45	236
4.61	0.50	-4.70	1643	49	214
4.59	0.47	-4.79	1562	55	205
4.56	0.44	-4.89	1524	62	197
4.54	0.42	-5.00	1460	72	189
4.53	0.41	-5.09	1281	80	182
4.52	0.40	-5.16	1223	83	178
4.50	0.39	-5.29	1268	93	170
4.49	0.37	-5.50	1612	111	156
4.47	0.36	-5.70	1290	131	146
4.47	0.36	-5.89	1705	138	140
4.46	0.35	-6.09	1978	138	131
4.46	0.35	-6.29	2005	139	126
4.45	0.34	-6.50	2022	139	119
4.45	0.34	-6.70	2248	139	122

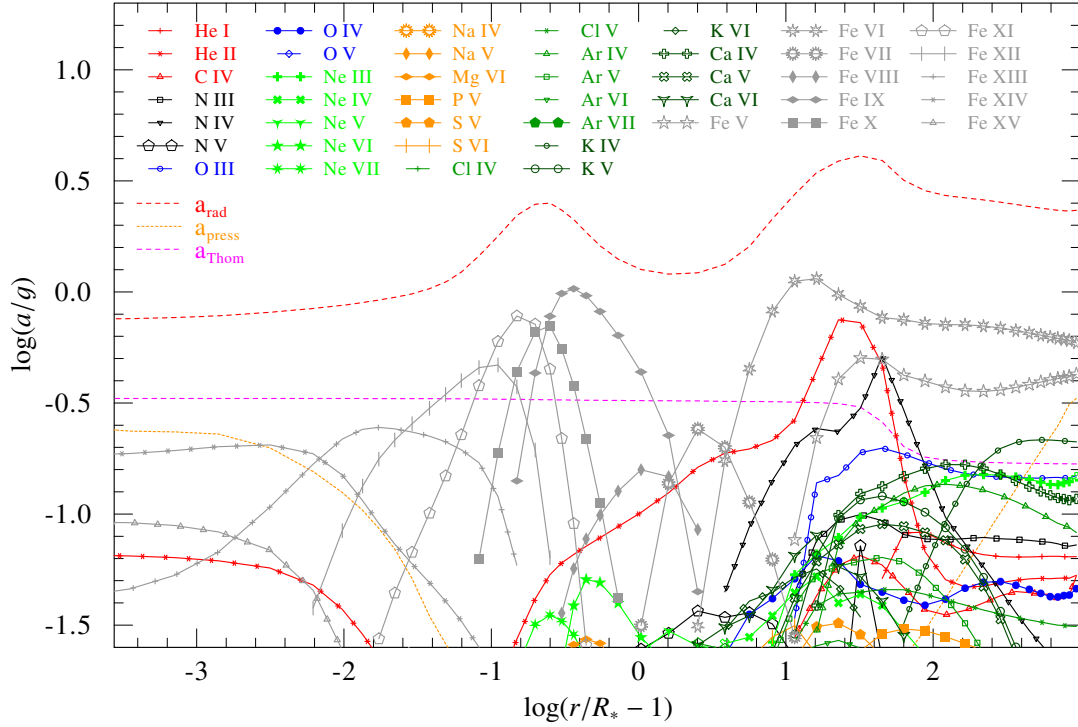


Figure 13. Contributions of the different ions to the radiative acceleration of a hydrodynamically consistent WN model with $T_* = 141$ kK, $\log L/L_\odot = 5.45$, $M_* = 13 M_\odot$, and $\log \dot{M} = -5.0$. All contributions with more than $\Gamma_{\text{ion}} = a_{\text{ion}}/g > 0.02$ are shown with different ions indicated by a combination of different color and symbol. For comparison, the total radiative acceleration (a_{rad}), the Thomson acceleration from free electrons, and the contribution from gas (and turbulence) pressure are also shown.

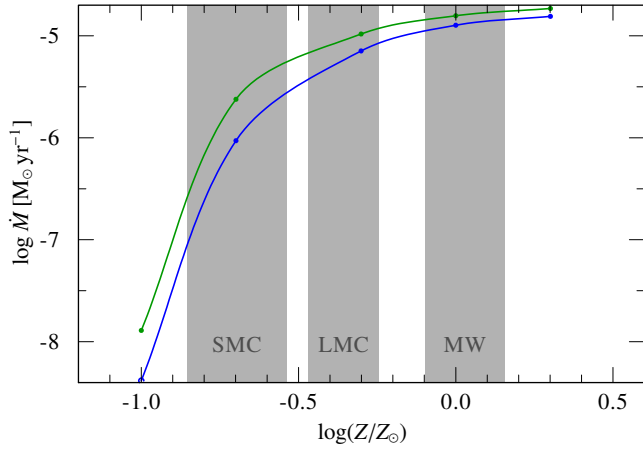


Figure 14. $\dot{M}(Z)$ for hydrodynamically consistent WN (green) and WC (blue) stars with fixed $\log L/L_\odot = 5.45$, $M_* = 11.5 M_\odot$, and $T_* = 141$ kK.

4.4 Mass loss vs. Gamma

For our investigation of $\dot{M}(\Gamma_e)$, we calculated four sequences of hydrodynamically consistent models. For Z_\odot and $0.1 Z_\odot$, we each calculated a series of WN and WC models. The obtained parameters are listed in Table 2 and the results in the \dot{M} - Γ_e -plane are shown in Fig. 15. As expected, there is a shift to higher Γ_e for the models with $0.1 Z_\odot$, while the overall behaviour of the four curves looks very similar. When the winds become thinner, implying lower \dot{M} , the gradient of all curves are increasing significantly. The curves at $0.1 Z_\odot$ are steeper than the ones at Z_\odot .

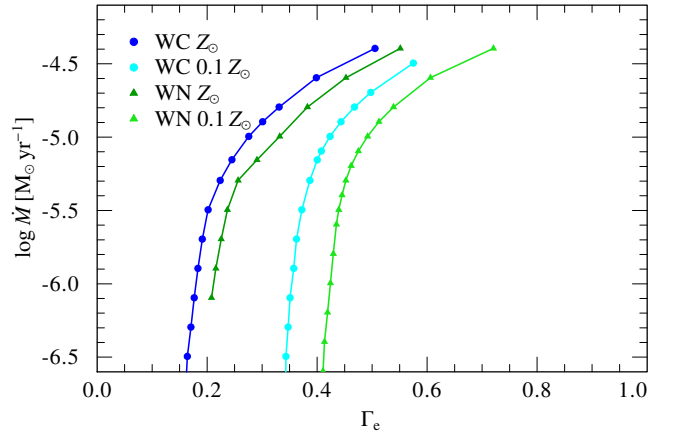


Figure 15. $\dot{M}(\Gamma_e)$ and for different hydrodynamically consistent models at solar metallicity and at $0.1 Z_\odot$. All models use $T_* = 141$ kK.

4.4.1 Transition to the optically thin wind regime

For lower \dot{M} , the wind configuration changes significantly as illustrated in Fig. 16, where we show the contributing ions for a WC model with a rather thin wind corresponding to a mass-loss rate of $\log \dot{M} = -6.1$. The comparison with Fig. 13 shows a substantial change of the ionization stages with Fe IX now being the leading contributor from the onset of the wind far out until transitioning to Fe VIII. The ‘dip’ between the two bumps is essentially gone as Fe VIII is now a significant driving contributor which was not the

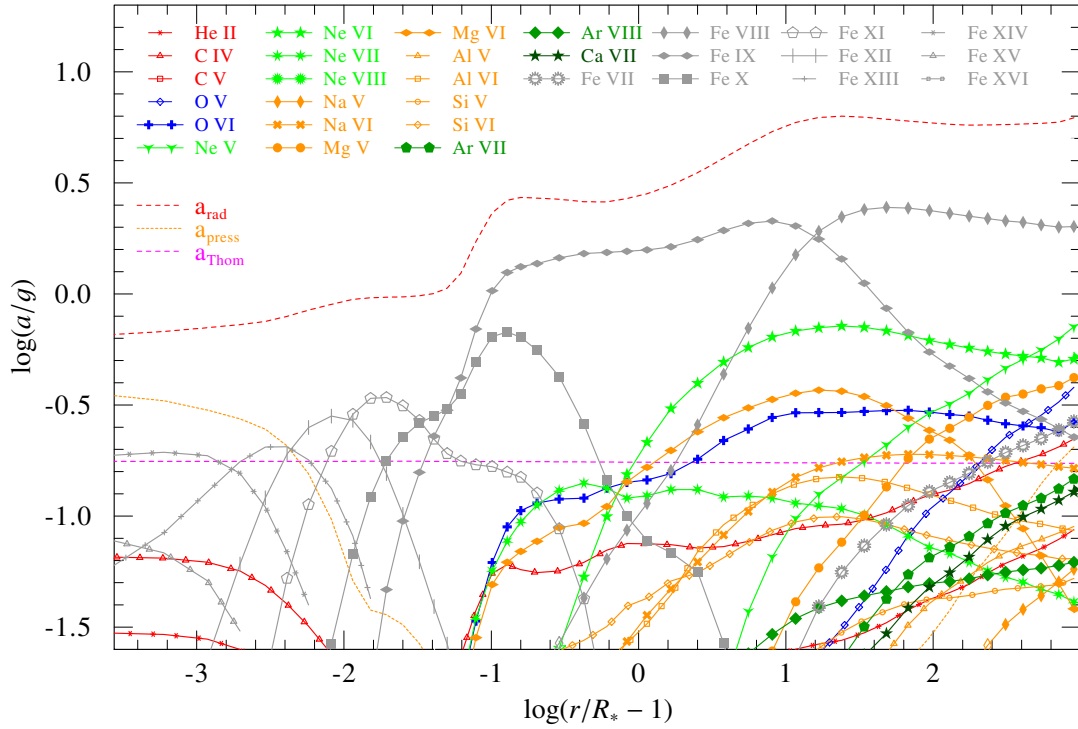


Figure 16. Contributions of the different ions to the radiative acceleration of a hydrodynamically consistent WC model with $T_* = 141$ KK, $\log L/L_\odot = 5.45$, $M_* = 19.4 M_\odot$, and $\log \dot{M} = -6.1$. All contributions with more than $\Gamma_{\text{ion}} = a_{\text{ion}}/g > 0.02$ are shown with different ions indicated by a combination of different color and symbol. For comparison, the total radiative acceleration (a_{rad}), the Thomson acceleration from free electrons, and the contribution from gas (and turbulence) pressure are also shown.

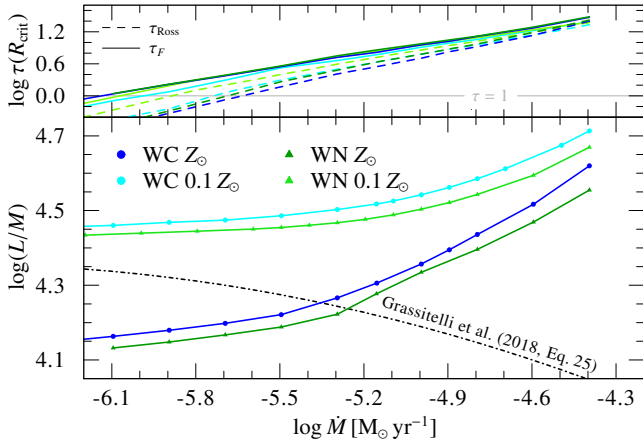


Figure 17. Lower panel: L/M_* versus \dot{M} for different hydrodynamically consistent models at solar metallicity and $0.1 Z_\odot$ (indicated by lighter colors). The prediction for the minimum L/M_* for a given \dot{M} by Grassitelli et al. (2018) in the case of a wind being driven by the hot iron bump at Z_\odot is drawn as a dashed-dotted line. Upper panel: Wind optical depth $\tau_F(R_{\text{crit}})$ and $\tau_{\text{Ross}}(R_{\text{crit}})$ for each model series as a function of the mass-loss rate \dot{M} .

case in the thick wind situation. This goes along with a higher electron temperature in the outer regions of the thin wind model.

The finding of thin-wind solutions launched at the hot iron bump could be seen as a contradiction of recent predictions based on stellar structure calculations by Grassitelli et al. (2018) and semi-analytic models based on OPAL tables by Ro (2019). Both works concluded that below a certain \dot{M} the hot iron bump would

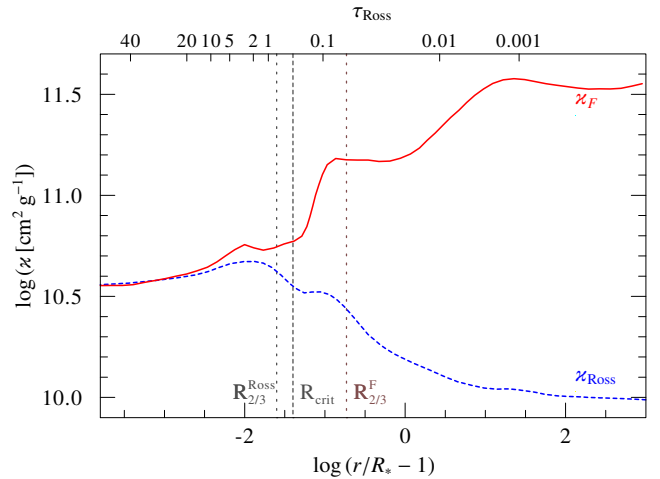


Figure 18. Comparison of the flux-weighted mean opacity (red, solid) with the Rosseland mean opacity (blue, dashed) for the WC model with the driving stratification depicted in Fig. 16 with $\log \dot{M} = -6.1$ and $Z = Z_\odot$.

lead to an inflation of the envelope while only becoming supersonic way further out. Instead, our WN and WC model sequences at Z_\odot pass smoothly through this precipitated limit as depicted in Fig. 17. An inspection of the model stratifications show that our findings for the model with $\log \dot{M} = -6.1$ are representative for all sequences with a rather smooth transition to different ionization stages in the wind. Given the very flat slope of $\log L/M_*$ vs. $\log \dot{M}$ at the low \dot{M} end in Fig. 17, however, the observed change in \dot{M} for a minor step

in L/M_* is quite drastic. Thus, for the values of L and M_* realized in nature there could indeed be an abrupt transition in \dot{M} .

As shown in the upper panel of Fig. 17, the optical depth of the wind denoted by $\tau_F(R_{\text{crit}})$ is smoothly decreasing with lower \dot{M} , indicating no abrupt regime change. Instead, we obtain an essentially linear relation between $\log \tau_F(R_{\text{crit}})$ and $\log \dot{M}$. The regime of the limit predicted by Grassitelli et al. (2018), corresponding to $\log \dot{M} \approx -5.3$ to -5.5 , does not exactly coincide with $\tau_F(R_{\text{crit}})$ passing unity, but there is a switch from Fe VI to Fe VII as the leading driver in the outer wind. The transition to an optically thin wind seems to happen rather gradually than abrupt. As illustrated in Fig. 18, where we show the two mean opacities similar to Fig. 2, now for our previously discussed thin-wind WC model, the critical point is no longer in the optically thick regime. Therefore the assumption of $\kappa_{\text{Ross}} = \kappa_F$ and thus the use of OPAL opacity tables is no longer valid at the base of the wind, explaining why we obtain solutions in contrast to Grassitelli et al. (2018) and Ro (2019). We do not have a comprehensive set of WR models with LMC metallicity in this work, but our findings indicate that if there is no abrupt minimum \dot{M} in terms of hydrodynamics for classical WR stars, the suggested decrease of the clumping factor by Ro (2019) for the early-type WR stars in LMC is probably not needed. Regarding their spectroscopic appearance, all of the models at $\log \dot{M} = -6.1$ still show major optical emission lines, although weaker than usual for early WR subtypes. Nonetheless, they would be spectroscopically classified as WR stars. Only models with a much lower $\log \dot{M} \approx -6.8$ would probably qualify for a transition type classification.

The switch to Fe VII (and then Fe VIII at even lower \dot{M}) as the main driver in the outer wind coincides with the wind – unlike at higher \dot{M} – also being no longer optically thick in the EUV range for hundreds of stellar radii. The lower wind densities allow the He II ionizing photons to escape, making helium stars with thin winds huge contributors of He II ionizing flux with $\log Q_{\text{He II}} = 48.3$ in the case of our models with $\log L/L_\odot = 5.45$ and $\log \dot{M} = -6.1$. While this mass-loss rate might be too low for the typical WN and WC star in our Galaxy, stripped He stars of lower masses – e.g. resulting from binary evolution – will have similar or even lower values of Γ_e and thus provide an enormous amount of hard ionizing flux. Recently, Göteborg et al. (2018) have calculated a series of models for stripped He stars. Their most massive model assumes $\log \dot{M} = -5.8$ and has $\log L/M_* = 4.07$, which is slightly below our calculated regime. Given our results, their assumption for \dot{M} would be too high (see also Vink 2017), meaning that their He II ionizing flux, which is about two orders of magnitude lower than their H I ionizing flux, is still underestimated by an order of magnitude. However, their value for T_* is a bit lower than ours and more tailored models will be required to further constrain the wind and ionizing flux situation for stripped helium stars of a lower luminosity (and mass) range.

Given that T_* and L are kept fixed in the calculations of our sequences, lower values of Γ_e imply higher masses and thus higher values of $g_* = GM_*R_*^{-2}$. As a consequence, the location of the critical point R_{crit} is moving further out as more gravity has to be overcome. Looking back at the slope of Γ_{rad} for the high-density models (see, e.g., Figs. 1, 4 or 13), one might expect that below a certain \dot{M} we could enter the regime of multiple critical points. This means as R_{crit} would eventually ‘climb up’ the hot iron bump, it could lead to regions with $\Gamma_{\text{rad}} < 1$ further out. In this case one would encounter a situation with $\Gamma_{\text{rad}} < 1$ in the innermost layers, transitioning to an acceleration region with $\Gamma_{\text{rad}} > 1$, then followed by a deceleration region with $\Gamma_{\text{rad}} < 1$, until eventually transitioning back to an

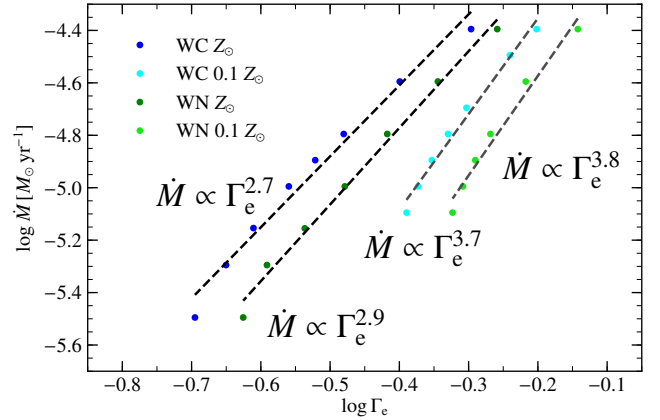


Figure 19. Linear fit to $\log \dot{M}$ versus $\log \Gamma_e$ for the upper part of the data depicted in Fig. 15.

accelerating wind with $\Gamma_{\text{rad}} > 1$. Neither physical, nor mathematical constraints forbid this and it might very well be realized in some WR winds in nature. Multiple locations with $\Gamma = 1$ imply either an inflated envelope (see e.g. the discussion in Grassitelli et al. 2018) or a deceleration region in the wind. Both would coincide with a non-monotonic $v(r)$, which can happen in our hydrodynamic solution, but would then be inhibited to avoid problems in the following CMF radiative transfer. Indeed some calculations run into this situation, depending on the chosen start approximation. However, when calculating our models with $T_* = 141$ kK in sequence, always using the last model as a start, we find our previously described solutions with a monotonic $v(r)$. While R_{crit} gets slightly larger with lower \dot{M} , the models are also not (significantly) inflated as the radiative acceleration changes its slope when the wind becomes optically thin. Thus, the whole solution topology remains in a situation with just one critical point. Future research will have to check whether the avoidance of multiple critical points is limited to a narrow parameter range (e.g. the selected T_* - and L -regime) or a more generally occurring phenomenon.

4.4.2 Fit relations for the mass-loss

For the classical WR stars, we can try to derive simple relations of the type $\dot{M} \propto \Gamma_e^x$ by forcing a linear fit in the log-log-Domain. This is depicted in Fig. 19, where we obtain very similar slopes for the WC and WN stars at Z_\odot with the WNs being potentially slightly steeper. For the sample at $0.1 Z_\odot$, we get steeper slopes than for Z_\odot . The data points also clearly indicate that the actual trend for $\dot{M}(\Gamma_e)$ is non-linear and we need to consider higher orders if we want to obtain a recipe for a broader range of mass-loss rates.

The dependency on Γ_e is so steep that a good fit could not be obtained in a double-logarithmic plane. Instead we derived a 3rd-order polynomial representation of \dot{M} vs. $\log \Gamma_e$, i.e.

$$\dot{M} = a_0 + a_1 \log \Gamma_e + a_2 (\log \Gamma_e)^2 + a_3 (\log \Gamma_e)^3 \quad (17)$$

with the coefficients given in Table 3. While this formula provides a decent description within the range of covered parameters, simple extrapolations are not encouraged, in particular towards higher Γ_e , as illustrated by the gray dashed lines in Fig. 20. The extrapolated range would predict a crossover of the relations for the WN and WC stars at Z_\odot , which is unlikely given the similar wind launching mechanism. As discussed at the beginning of Sect. 4, the higher

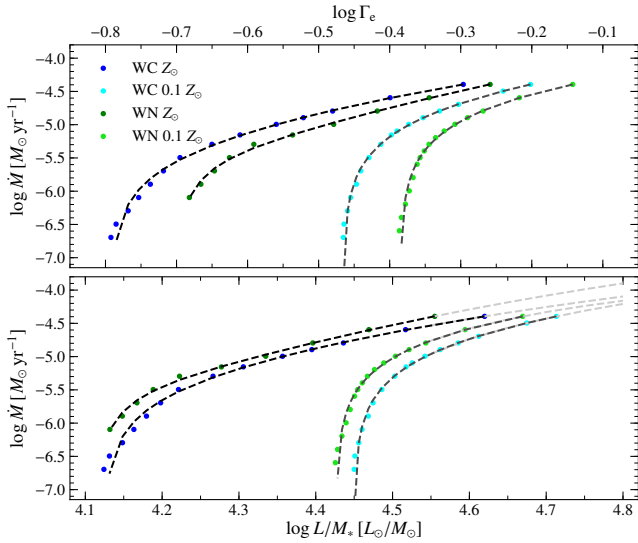


Figure 20. Nonlinear fit to $\log \dot{M}$ versus $\log \Gamma_e$ (upper panel) and $\log L/M_*$ (lower panel) for the WN and WC models from Table 2 with extrapolation denoted in grey.

Table 3. Analytic fit for the mass-loss rate dependency

	Z [Z_\odot]	a_0 [10^{-4}]	a_1 [10^{-4}]	a_2 [10^{-4}]	a_3 [10^{-4}]
\dot{M} vs. $\log \Gamma_e$					
WN	1.0	1.334	5.293	7.569	3.900
WN	0.1	0.718	2.301	0.261	-2.255
WC	1.0	1.166	3.555	3.717	1.373
WC	0.1	0.943	3.182	2.411	-0.156
\dot{M} vs. $\log L/M_\odot$					
WN	1.0	-284.175	203.817	-48.819	3.905
WN	0.1	247.954	-157.529	32.964	-2.266
WC	1.0	-89.923	66.773	-16.582	1.377
WC	0.1	62.349	-32.002	4.749	-0.159

values of \dot{M} for the WC stars compared to the WN stars of the same Γ_e are an effect of the ionization parameter q_{ion} , which – in the inner part – is ≈ 0.39 for our WC and ≈ 0.49 for our WN models.

To illustrate the effect of higher mass-loss rates for WC stars compared to WN stars with the same L and M , as well as to avoid the need for requiring q_{ion} in order to get to the fundamental stellar parameters, we also derive relations for \dot{M} as a function of $\log L/M_*$, again using a 3rd-order polynomial, i.e.

$$\dot{M} = a_0 + a_1 \log \frac{L}{M_*} + a_2 \left(\log \frac{L}{M_*} \right)^2 + a_3 \left(\log \frac{L}{M_*} \right)^3 \quad (18)$$

with L and M_* being given in solar units and \dot{M} in $M_\odot \text{yr}^{-1}$. The coefficients a_i are given in the lower part of Table 3 and the curves are illustrated in the lower panel of Fig. 20. The relations derived here are a bit more robust with higher orders having smaller coefficients and the extrapolations yield more reasonable results than in the Γ_e -description.

A first glimpse of how our relations for $\dot{M}(\Gamma_e)$ perform in comparison to observations is shown in Fig. 21. Here, we compare a sample of hydrogen-free WR stars using the recent empirical results from Hamann et al. (2019) and Sander et al. (2019) where

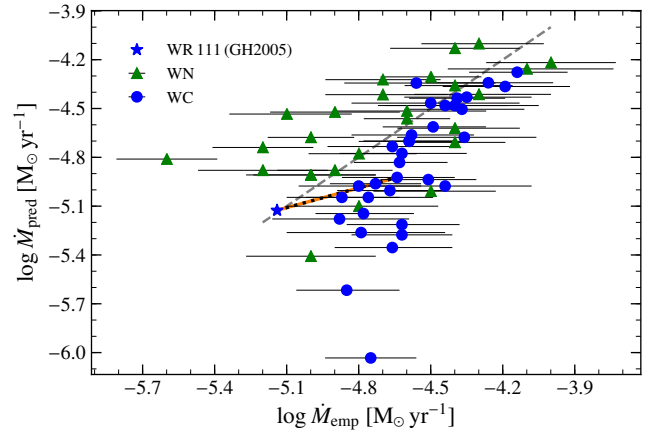


Figure 21. Comparison of the empirically derived \dot{M} for hydrogen-free WR stars from Sander et al. (2019) and Hamann et al. (2019) with predictions for $\dot{M}(L/M_*)$ using the coefficients from Tab. 3. The hydrodynamically consistent modelling of WR 111 from GH2005 is also shown, using the updated L (and resulting M_*) based on Gaia DR2 distance in the fit formula. The black dotted line on an orange background connects this result with the empirical solution from Sander et al. (2019).

the luminosities and mass-loss rates have been updated based on Gaia DR2 parallaxes. For comparison, we also show the result for WR 111 from GH2005. The value we obtain with our formula and the L/M_* based on Sander et al. (2019) agrees nicely with their tailored result. This is not a surprise as our model series was motivated on their parameter set, but given all the differences in the details it is also a nice sanity check. The remaining sample in Fig. 21 is based on purely empirical approaches where simply β -laws were adopted for the velocity stratification.

Given the fact that our comparison data stems from a grid analysis, we estimate a systematic uncertainty of 0.15 dex – reflecting the difference between two grid models – for the empirical mass-loss rates, which we add to the errors from the distance uncertainty. As we see in Fig. 21, even with these rather generous errors, several stars do not touch the identity relation. The two strongest outliers are the weak-lined and peculiar WN3 star WR 46, which might not be a single star as discussed in Hamann et al. (2006), potentially explaining the apparently low empirical \dot{M} , and the WC4 star WR 52, for which we predict an \dot{M} that is an order of magnitude too low. Although not a drastic as for WR 46, several weak-lined WNs get much higher predictions for \dot{M} than observed, hinting that either our assumptions in this work are not valid for this type of stars, or their lines might be diluted by a yet undetected companion. WR 52 has a very high wind efficiency with $\eta \approx 24$ in Sander et al. (2019), more than twice the value that WR 111 has in the same study. One solution could be that WR 52 is more evolved and the mass of $8.5 M_\odot$ deduced from the luminosity in Sander et al. (2019) is overestimated. However, for the shift of about one magnitude in \dot{M} , the mass would need to go down by about a factor two, which is hard to justify. An underestimation of the luminosity would be more plausible, but the rather well constrained parallax in Gaia DR2 also puts doubts on this. Here, and also for the scatter of the other objects, we need to keep in mind that in this work we only have models for one T_* and \dot{M} will not only change with L , M , and X_i , but also T_* . Nonetheless, the overall agreement is promising and hints that at least a good part of the Galactic WR population could be compact He stars with a dense, complex wind structure. Still, the difference

between the empirically deduced result for WR 111 and the tailored hydrodynamical model (illustrated by a black line connecting the data points in Fig. 21) makes it clear that even in this case there is probably no simple ‘correction formula’. In other words, parameters derived from an HD analysis will differ in varying magnitude between different WR stars, indicating that really a new generation of atmosphere models is needed to properly constrain the stellar parameters of classical WR stars.

4.5 The velocity profile

The velocity profile obtained in our hydrodynamically consistent models reflect the complex shape of Γ_{rad} . An example for a WC model is shown in the left panel of Fig. 22, where we compare the consistent solution to different β -laws smoothly connected to a hydrostatic part. In the outer wind, the HD solution reprises a β -law, but the increase in the inner wind is steeper than any β -type velocity law and the decrease of the radiative acceleration between the two main bumps leads to a bump in $v(r)$ as well. These results are in line with the findings of GH2005, stating that none of the currently used analytic approximations accurately reflect the velocity field of their model for WR 111. We can now extend this conclusion to the whole regime of classical WR stars, as we illustrate in the central panel of Fig. 22, where the velocity profiles from various WN models with different mass-loss rates are shown. With the exception of the lowest \dot{M} , all models show a structure with bumps or plateaus for $v(r)$. The closer Γ_{rad} gets back to unity after the hot iron bump, the more plateau-like the velocity profile will become. Only when the ionization structure changes to the thin-wind situation discussed above in Sect. 4.4, $v(r)$ returns to a more standard, β -like behavior.

Aside from lower wind densities, the ‘bumpy’ structure of the velocity profile also becomes weaker and eventually vanishes when transitioning to lower metallicities. This is a straight-forward consequence of the lower Fe abundance since the first increase of $v(r)$ is caused by the opacities of Fe IX to Fe XVI (cf. Figs. 5 and 13). For models with the same \dot{M} , the imprint of the hot iron bump is noticeable in the velocity structure until $Z < 0.1 Z_{\odot}$ (cf. right panel of Fig. 22). Another consequence of the lower Z is the decrease of v_{∞} , which eventually stalls when the wind acceleration is maintained by continuum driving (cf. Sect. 4.3.1). From the perspective of constant L/M , we see a different trend for v_{∞} in Fig. 23. Our test model series with $\log L/L_{\odot} = 5.45$ and $M_{*} = 11.5 M_{\odot}$ (cf. Sect. 4.3.2) predicts only a decrease in v_{∞} down to LMC metallicities for WCs and down to SMC metallicities for WNs. At even lower Z , where \dot{M} drops by orders of magnitude, we find a sharp increase in v_{∞} . With lower Z , less radiative cooling is available, and higher ions such as e.g. Fe IX or Ne VII stay significantly populated throughout the wind, boosting the acceleration despite their lower abundances. A higher v_{∞} would also provide a first, qualitative, explanation to why Vink & de Koter (2005) find a less steep decrease in \dot{M} . In their global Monte Carlo approach, they fix v_{∞} and derive

$$\dot{M} = \frac{2\Delta L}{v_{\infty}^2 + v_{\text{esc}}^2} \quad (19)$$

with ΔL being the luminosity removed between the hydrostatic layers and infinity due to the acceleration of the stellar wind. From Eq. (19) it is immediately clear that an underestimation of v_{∞} would lead to an overestimation in \dot{M} . A quick scaling shows that this would not be able to account for the full difference, but as the models from Vink & de Koter (2005) are for late-type WR stars, the quantitative comparison might be biased. Newer calculations

with Monte Carlo models based on the approach by Müller & Vink (2008) have been performed for a series of He star models in Vink (2017) include a prediction of v_{∞} based on a semi-analytic expression for the line acceleration, which we discussed in Sect. 3. There are no direct matches in terms of stellar parameters between the sets in Vink (2017) and our $\dot{M}(Z)$ sequence, but we can use their results for the $15 M_{\odot}$ star at $0.33 Z_{\odot}$ and $0.1 Z_{\odot}$ for a rough comparison. At $0.33 Z_{\odot}$, the mass-loss rates are lower than in our case, but at $0.1 Z_{\odot}$ they are considerably higher. Given that Vink (2017) used a temperature of 50kK in the Monte Carlo calculations, this does not tell much, apart from reflecting that the metallicity trends for helium stars are highly uncertain. This is even more true for the terminal velocities, where none of the sequences in Vink (2017) shows an increase for v_{∞} at sub-LMC metallicity. Recent models by Vink (2018) for very massive and rather cool (15kK) stars also showed that v_{∞} is not simply decreasing with lower Z , but their minimum is located at way lower metallicities ($0.03 Z_{\odot}$) than in our series.

Given the complex shapes of $v(r)$, an in-depth analysis of its behaviour and a physically motivated analytical recipe for $v(r)$ is – despite the high scientific demand, for example for the accurate time-dependent modelling of WR winds – a whole study of its own, which we have to leave as an important future follow-up.

5 CONCLUSIONS

In this work we have introduced a series of next-generation stellar atmosphere models for classical Wolf-Rayet stars of WN and WC type. The velocity stratification is obtained by solving the hydrodynamic equation of motion, thus being locally dynamically consistent throughout the whole atmosphere in contrast to previous, e.g. Monte Carlo based, models, with the exception of the prototypical study by GH2005. Our examination of the resulting radiative acceleration yields a total breakdown of CAK-like descriptions. Neither the CAK optical depth parameter, nor the force multiplier itself turn out to be monotonic functions of radius or optical depth. Moreover, bound-free and free-free contributions cannot be neglected.

All winds in our study are launched by the opacities of Fe M-shell ions. The complex ionization structure is imprinted in the velocity profile in the form of ‘bumps’ or plateaus, causing significant deviations from β -type velocity laws. In line with the prototypical result for WR 111 from GH2005, we assume a depth-dependent clumping with $D_{\infty} = 50$ in the outer wind and derive that neither a β , nor a 2β -law accurately reprises the derived $v(r)$, especially not in the inner part of the wind. At typical mass-loss rates, the winds of classical WR stars can be optically thick with regards to τ_{Ross} for a few stellar radii. The optical depth τ_F defined by the flux-weighted mean opacity is even larger, reflecting that the wind is ‘optically thick’ with regards to driving. The radius where τ_F drops below $2/3$ is usually an order of magnitude larger than for τ_{Ross} . Our assumed $D_{\infty} = 50$ is on the high end of what has been empirically derived. Compared to the more conservative $D_{\infty} = 10$, our v_{∞} is about 30% higher. \dot{M} however, is set in a region barely affected by D_{∞} . Thus, we consider our derived trends robust against changes of D_{∞} , but recommend further studies on the impact of clumping.

We obtain a steep dependence between \dot{M} and Γ_e or $\log L/M$ for both WN and WC stars. Tests show only a weak additional L -dependence, making L/M the crucial quantity. For WC stars, larger C or O mass fractions lead to a decrease in \dot{M} for constant L and M_{*} . To maintain a certain \dot{M} at lower metallicity, stars have to get closer to the Eddington limit as the line opacities diminish. All

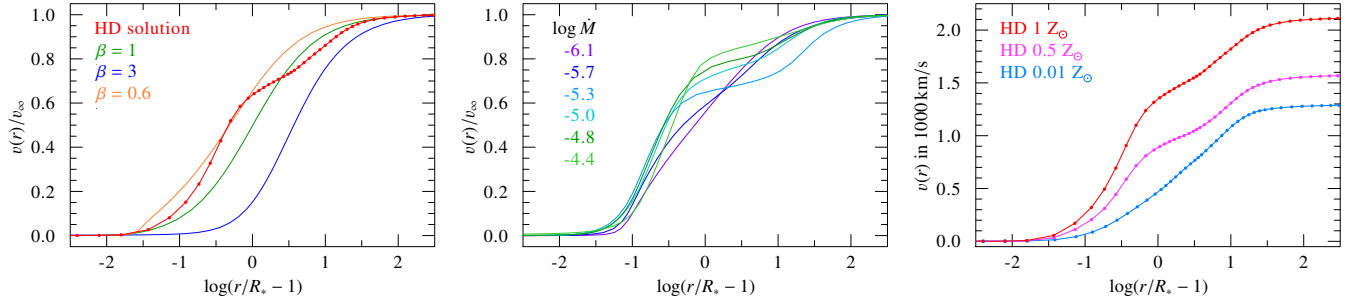


Figure 22. Normalized velocity profile $v(r)/v_\infty$ for a WC model with $\log \dot{M} = -5.15$ at Z_\odot compared to non-HD models using different β -laws (left panel) and for WN models with different \dot{M} at Z_\odot (middle panel). The right panel depicts the absolute $v(r)$ for WC stars with the same L and \dot{M} at different Z

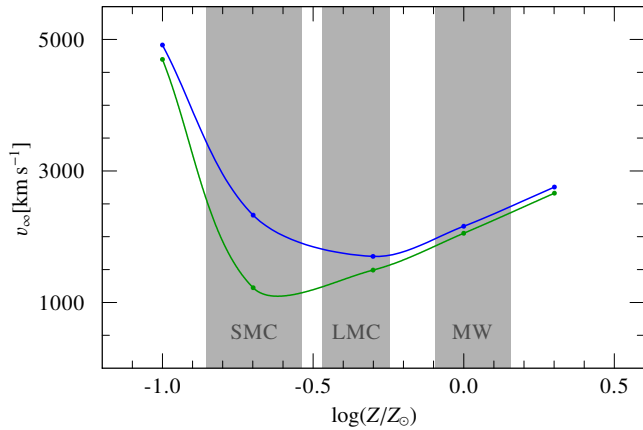


Figure 23. $v_\infty(Z)$ for WN (green) and WC (blue) models at different metallicity Z with the same L and M_*

types of continuum opacities then take part in maintaining the wind acceleration, more pronounced in the case of WC stars.

Our finding that the optically thick winds of potentially all types of classical WR stars can be launched at the so-called ‘hot iron bump’ matches with the conclusions from recent hydrodynamic stellar structure calculations (Grassitelli et al. 2018) as long as $\tau_F(R_{\text{crit}}) \gg 1$, paving the way for an agreement between wind and structure models for He stars after decades of severe disagreement. However, we also do find solutions for winds launched below the \dot{M} -limit recently suggested on the basis of OPAL opacity tables. For lower \dot{M} , the leading ionization in the outer stellar wind switches to higher Fe ions and the winds become optically thin, making the approach of using Rosseland opacities as a proxy for flux-mean opacities invalid. Given the steep slope of our \dot{M} -predictions for low L/M , we cannot exclude an abrupt transition in the observed properties of He stars and their conditions at the base of the wind. In the larger context, the caveats of hydrostatic structure models and our results derived in this work call for a unified approach where the subsonic stellar structure and the supersonic wind are treated consistently. We plan to study next-generation models of He stars in a more coherent context in a follow-up study, including their emergent spectra and detailed ionizing fluxes. So far, our results indicate that the presently assumed He II ionizing fluxes for stripped He stars might still be underestimated due to an overestimation of their mass-loss rate \dot{M} .

We did a first comparison between the \dot{M} -predictions based on our new models with empirically derived \dot{M} values using traditional stellar atmospheres with prescribed β -laws for the wind velocity.

We obtain a considerable scatter, illustrating that the present approaches of analysing classical WR stars likely have severe shortcomings with regards to the derived stellar parameters. As their spectra are originating in the rapid wind layers, hydrodynamically consistent models are the only way to break existing parameter degeneracies.

We also calculated a test series of models to study the mass-loss rate of WR stars with constant Γ_e at different Z . The results indicate a breakdown of \dot{M} by about two orders of magnitude between 0.2 and $0.1 Z_\odot$. This is significantly more than deduced by Vink & de Koter (2005) and would allow for massive stars below $0.2 Z_\odot$ to form black holes with higher masses than currently assumed, potentially having considerable effects on gravitational wave statistics.

ACKNOWLEDGEMENTS

The authors would like to thank the referee, L. Grassitelli, for fruitful comments and suggestions that helped to improve the manuscript. A.A.C.S. and J.S.V. are supported by STFC funding under grant number ST/R000565/1. W.-R.H. acknowledges support from the Deutsche Forschungsgemeinschaft under grant HA 1455/26. We further acknowledge helpful discussions with G. GrÅd’fener, L.M. Oskinova, H. Todt, R. Hainich, and T. Shenar.

REFERENCES

- Abbott D. C., Lucy L. B., 1985, *ApJ*, **288**, 679
 Abbott B. P., et al., 2016, *ApJ*, **818**, L22
 Beals C. S., 1929, *MNRAS*, **90**, 202
 Belczynski K., Bulik T., Fryer C. L., Ruitter A., Valsecchi F., Vink J. S., Hurley J. R., 2010, *ApJ*, **714**, 1217
 Bestenlehner J. M., et al., 2014, *A&A*, **570**, A38
 Bouret J.-C., Hillier D. J., Lanz T., Fullerton A. W., 2012, *A&A*, **544**, A67
 Cantiello M., et al., 2009, *A&A*, **499**, 279
 Castor J. I., Abbott D. C., Klein R. I., 1975, *ApJ*, **195**, 157
 Chen Y., Bressan A., Girardi L., Marigo P., Kong X., Lanza A., 2015, *MNRAS*, **452**, 1068
 Crowther P. A., 2007, *ARA&A*, **45**, 177
 Crowther P. A., Schnurr O., Hirschi R., Yusof N., Parker R. J., Goodwin S. P., Kassim H. A., 2010, *MNRAS*, **408**, 731
 Eldridge J. J., Fraser M., Smartt S. J., Maund J. R., Crockett R. M., 2013, *MNRAS*, **436**, 774
 Friend D. B., Abbott D. C., 1986, *ApJ*, **311**, 701
 Gayley K. G., Owocki S. P., Cranmer S. R., 1995, *ApJ*, **442**, 296
 Georgy C., Ekström S., Meynet G., Massey P., Levesque E. M., Hirschi R., Eggenberger P., Maeder A., 2012, *A&A*, **542**, A29
 Gilkis A., Vink J. S., Eldridge J. J., Tout C. A., 2019, *MNRAS*, **486**, 4451

- Götberg Y., de Mink S. E., Groh J. H., Kupfer T., Crowther P. A., Zapartas E., Renzo M., 2018, *A&A*, **615**, A78
- Gräfener G., Hamann W.-R., 2005, *A&A*, **432**, 633
- Gräfener G., Hamann W.-R., 2008, *A&A*, **482**, 945
- Gräfener G., Koesterke L., Hamann W.-R., 2002, *A&A*, **387**, 244
- Gräfener G., Vink J. S., de Koter A., Langer N., 2011, *A&A*, **535**, A56
- Gräfener G., Owocki S. P., Vink J. S., 2012, *A&A*, **538**, A40
- Gräfener G., Owocki S. P., Grassitelli L., Langer N., 2017, *A&A*, **608**, A34
- Grassitelli L., Fossati L., Simón-Díaz S., Langer N., Castro N., Sanyal D., 2015, *ApJ*, **808**, L31
- Grassitelli L., Chené A.-N., Sanyal D., Langer N., St-Louis N., Bestenlehner J. M., Fossati L., 2016, *A&A*, **590**, A12
- Grassitelli L., Langer N., Grin N. J., Mackey J., Bestenlehner J. M., Gräfener G., 2018, *A&A*, **614**, A86
- Groh J. H., Meynet G., Georgy C., Ekström S., 2013, *A&A*, **558**, A131
- Hainich R., Pasemann D., Todt H., Shenar T., Sander A., Hamann W.-R., 2015, *A&A*, **581**, A21
- Hamann W.-R., Gräfener G., 2003, *A&A*, **410**, 993
- Hamann W., Koesterke L., 1998, *A&A*, **335**, 1003
- Hamann W., Gräfener G., Liermann A., 2006, *A&A*, **457**, 1015
- Hamann W.-R., et al., 2019, *A&A*, **625**, A57
- Iglesias C. A., Rogers F. J., 1996, *ApJ*, **464**, 943
- Jiang Y.-F., Cantiello M., Bildsten L., Quataert E., Blaes O., 2015, *ApJ*, **813**, 74
- Kato M., Iben Jr. I., 1992, *ApJ*, **394**, 305
- Krtićka J., Kubát J., 2011, *A&A*, **534**, A97
- Kudritzki R. P., 2002, *ApJ*, **577**, 389
- Kudritzki R.-P., Puls J., 2000, *ARA&A*, **38**, 613
- Kudritzki R. P., Springmann U., Puls J., Pauldrach A. W. A., Lennon M., 1998, in Howarth I., ed., *Astronomical Society of the Pacific Conference Series Vol. 131, Properties of Hot Luminous Stars*. p. 299
- Lamers H. J. G. L. M., Leitherer C., 1993, *ApJ*, **412**, 771
- Langer N., 1989, *A&A*, **210**, 93
- Liermann A., Hamann W.-R., Osinkova L. M., Todt H., Butler K., 2010, *A&A*, **524**, A82
- Limongi M., Chieffi A., 2018, *ApJS*, **237**, 13
- Lucy L. B., Abbott D. C., 1993, *ApJ*, **405**, 738
- Lucy L. B., Solomon P. M., 1970, *ApJ*, **159**, 879
- Mahy L., Rauw G., De Becker M., Eenens P., Flores C. A., 2015, *A&A*, **577**, A23
- Marchant P., Langer N., Podsiadlowski P., Tauris T. M., Moriya T. J., 2016, *A&A*, **588**, A50
- Martins F., Hillier D. J., Paumard T., Eisenhauer F., Ott T., Genzel R., 2008, *A&A*, **478**, 219
- McClelland L. A. S., Eldridge J. J., 2016, *MNRAS*, **459**, 1505
- Mendoza C., Nahar S., Pradhan A., Seaton M., Zeippen C., 2001, in *APS Division of Atomic, Molecular and Optical Physics Meeting Abstracts*. p. S5.079
- Mihalas D., Kunasz P. B., Hummer D. G., 1975, *ApJ*, **202**, 465
- Muijres L. E., Vink J. S., de Koter A., Müller P. E., Langer N., 2012, *A&A*, **537**, A37
- Müller P. E., Vink J. S., 2008, *A&A*, **492**, 493
- Noebauer U. M., Sim S. A., 2015, *MNRAS*, **453**, 3120
- Nugis T., Lamers H. J. G. L. M., 2000, *A&A*, **360**, 227
- Nugis T., Lamers H. J. G. L. M., 2002, *A&A*, **389**, 162
- Owocki S. P., 1994, in Balona L. A., Henrichs H. F., Le Contel J. M., eds., *IAU Symposium Vol. 162, Pulsation; Rotation; and Mass Loss in Early-Type Stars*. p. 475
- Pauldrach A., Puls J., Kudritzki R. P., 1986, *A&A*, **164**, 86
- Pistinner S., Eichler D., 1995, *ApJ*, **454**, 404
- Puls J., Springmann U., Lennon M., 2000, *A&AS*, **141**, 23
- Puls J., Vink J. S., Najarro F., 2008, *A&ARv*, **16**, 209
- Renzo M., Ott C. D., Shore S. N., de Mink S. E., 2017, *A&A*, **603**, A118
- Ro S., 2019, *ApJ*, **873**, 76
- Ro S., Matzner C. D., 2016, *ApJ*, **821**, 109
- Sander A., Hamann W.-R., Todt H., 2012, *A&A*, **540**, A144
- Sander A., Shenar T., Hainich R., Gímenez-García A., Todt H., Hamann W.-R., 2015, *A&A*, **577**, A13
- Sander A. A. C., Hamann W.-R., Todt H., Hainich R., Shenar T., 2017, *A&A*, **603**, A86
- Sander A. A. C., Fürst F., Kretschmar P., Osinkova L. M., Todt H., Hainich R., Shenar T., Hamann W.-R., 2018, *A&A*, **610**, A60
- Sander A. A. C., Hamann W.-R., Todt H., Hainich R., Shenar T., Ramachandran V., Osinkova L. M., 2019, *A&A*, **621**, A92
- Sanyal D., Langer N., Szécsi D., -C Yoon S., Grassitelli L., 2017, *A&A*, **597**, A71
- Schmutz W., Hamann W.-R., Wessolowski U., 1989, *A&A*, **210**, 236
- Vink J. S., 2000, PhD thesis, Universiteit Utrecht
- Vink J. S., 2006, in Lamers H. J. G. L. M., Langer N., Nugis T., Annuk K., eds., *Astronomical Society of the Pacific Conference Series Vol. 353, Stellar Evolution at Low Metallicity: Mass Loss, Explosions, Cosmology*. p. 113 ([arXiv:astro-ph/0511048](https://arxiv.org/abs/astro-ph/0511048))
- Vink J. S., 2017, *A&A*, **607**, L8
- Vink J. S., 2018, *A&A*, **615**, A119
- Vink J. S., Gräfener G., 2012, *ApJ*, **751**, L34
- Vink J. S., de Koter A., 2005, *A&A*, **442**, 587
- Vink J. S., de Koter A., Lamers H. J. G. L. M., 1999, *A&A*, **350**, 181
- Vink J. S., de Koter A., Lamers H. J. G. L. M., 2000, *A&A*, **362**, 295
- Vink J. S., de Koter A., Lamers H. J. G. L. M., 2001, *A&A*, **369**, 574
- Vink J. S., Muijres L. E., Anthonisse B., de Koter A., Gräfener G., Langer N., 2011, *A&A*, **531**, A132
- Vink J. S., et al., 2015, *Highlights of Astronomy*, **16**, 51
- Wolf C. J. E., Rayet G., 1867, *Academie des Sciences Paris Comptes Rendus*, **65**, 292
- Yoon S.-C., Gräfener G., Vink J. S., Kozyreva A., Izzard R. G., 2012, *A&A*, **544**, L11

APPENDIX A: THE BREAKDOWN OF CAK-LIKE DESCRIPTIONS FOR WR STARS

Theoretical modeling of the winds of hot massive O and WR stars has a long history. Following up on the suggestion that radiation intercepted by spectral lines could be sufficient to explain the driving of hot star winds (Lucy & Solomon 1970), the path-breaking work in this area was the CAK paper (after Castor, Abbott & Klein 1975) which developed the so-called CAK force-multiplier framework, describing the line force as an amplification of the electron scattering (Thomson) force by a force multiplier \mathcal{M} , involving both a line-strength parameter k , and a parameter α which reflects the distribution of optically thin to thick lines (e.g. Puls et al. 2000).

Neglecting bound-free and free-free contributions, the radiative acceleration in (m)CAK is written as

$$\Gamma_{\text{rad}}^{\text{CAK}} = (1 + \mathcal{M})\Gamma_e. \quad (\text{A1})$$

with the force multiplier \mathcal{M} (cf. Eq. B3) parametrized in the form

$$\mathcal{M}(t) = \hat{k}t^{-\alpha}\hat{n}^\delta \quad (\text{A2})$$

with the definitions

$$t := n_e(r)\sigma_e v_{\text{th,H}} \left(\frac{dv}{dr} \right)^{-1}, \quad (\text{A3})$$

$$\hat{n} := \frac{n_e(r)}{10^{-11} \text{ cm}^{-3}} \frac{1}{W(r)}, \quad \text{and} \quad (\text{A4})$$

$$W(r) := \frac{1}{2} \left(1 - \sqrt{1 - \left(\frac{R_*}{r} \right)^2} \right). \quad (\text{A5})$$

All quantities in Eq. (A2) are dimensionless and ideally, α and δ should be constant, at least throughout the wind. It is known for decades already that the latter is not the case, even in OB supergiants (e.g. Kudritzki et al. 1998; Vink 2000; Kudritzki 2002; Muijres et al. 2012). When plotting e.g. $\log \mathcal{M}$ versus $\log t$, the resulting curve is not a straight line, but instead requires a non-linear fit.

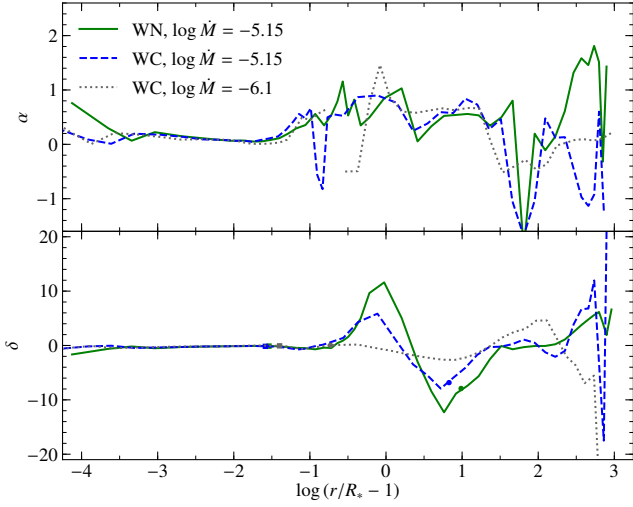


Figure A1. Effective force multiplier parameters α (upper panel) and δ (lower panel) as a function of radius for three different WR models (see Table 1 for detailed parameters). The squares denote the location of the critical point in the models while the dots mark $\tau_F = 2/3$.

While this makes the formula slightly less elegant, it still provides an efficient and fast way to properly describe the radiative force.

With our detailed calculation of the radiative acceleration in the CMF, we can test the validity of a description like in Eq. (A2) using the previous definitions and the obtained values for \mathcal{M} via Eq. (B3). The parameters α and δ can then be obtained via

$$\alpha(r) = -\frac{\partial(\log \mathcal{M})}{\partial(\log t)} \quad \text{and} \quad \delta(r) = -\frac{\partial(\log \mathcal{M})}{\partial(\log \hat{n})} \quad (\text{A6})$$

with $\hat{k}(r)$ then being determined via the obtained quantities and Eq. (A2). Such defined quantities are termed ‘effective’ force multiplier parameters as they are not based on an underlying line-strength distribution (cf. Puls et al. 2000). The original CAK concept treats \hat{k} , α , and δ as constant throughout the wind. This was relaxed in later extensions (e.g. Kudritzki 2002) to account for the fact that no lines with infinite strengths exist and thus $\mathcal{M}(t)$ eventually saturates. Since this depth-dependence can already be important for O stars, we do expect a depth-dependency for these parameters for WR stars, as already hinted by the results from GH2005.

The obtained behavior of $\alpha(r)$ and $\delta(r)$ for typical Galactic WN and WC models are depicted in Fig. A1. All curves in both graphs look very different from what is obtained for OB-type stars. In particular the part outwards from R_{crit} shows wild jumps for α . The δ parameter reflecting the ionization change has a smoother shape, but with a huge positive and negative amplitudes it by far exceeds the region of $0.0 \dots 0.2$ known in usual mCAK-descriptions.

A close inspection of the Sobolev optical depth parameter t in Fig. A2 reveals that t is not a monotonic representation of the optical depth scale (here τ_{Ross}) and thus $\mathcal{M}(t)$ is not a proper mathematical function, leading to the complete breakdown of the CAK theory. For a lower $\log \dot{M} = -6.1$, we find a monotonic relation. However, this does not lead to simple slopes for α and δ as in mCAK, but instead only reduces the amplitude of the scatter.

Alternatively to a straight-forward mCAK description, one could try to apply a general term containing the density and the velocity gradient following GH2005, i.e.

$$\mathcal{M} \propto \left(\frac{1}{\rho} \frac{dv}{dr} \right)^{\tilde{\alpha}} \equiv \tilde{t}^{\tilde{\alpha}}. \quad (\text{A7})$$

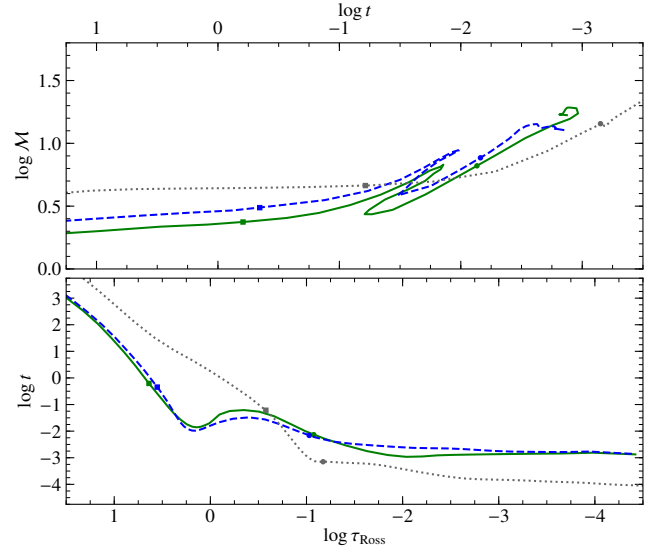


Figure A2. Upper panel: Force multiplier \mathcal{M} versus the Sobolev optical depth parameter t . Lower panel: Sobolev optical depth parameter t as a function of the Rosseland optical depth. (Same models as in Fig. A1)

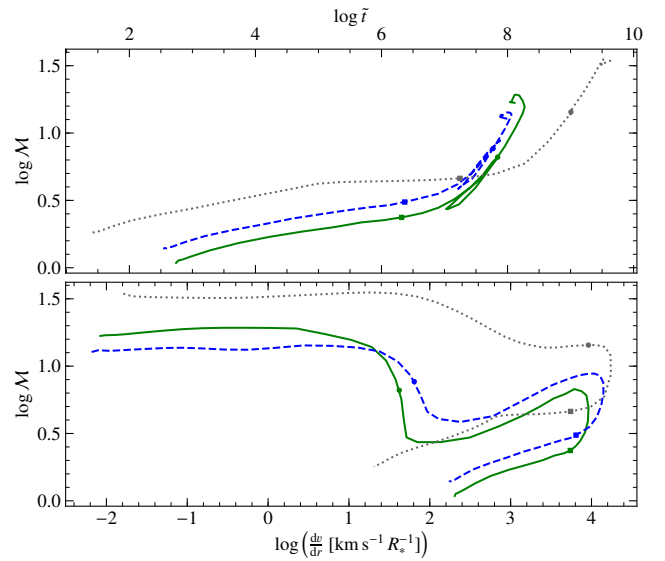


Figure A3. Force multiplier \mathcal{M} versus the depth parameter \tilde{t} from GH2005 (upper panel) and velocity gradient (lower panel) for the three different WR models specified in Table 1.

The resulting curve for $\mathcal{M}(\tilde{t})$ is shown in the upper panel of Fig. A3, revealing a non-monotonic behaviour of \tilde{t} for dense WR winds, similar to what we obtained for the mCAK description. More fundamentally, the force multiplier \mathcal{M} itself is not a monotonically increasing function, not even over the radius, not even in the outer wind where WR atmospheres behave more like OB atmospheres. In fact, we even see this in OB models, such as the HD calculations for ζ Pup (Sander et al. 2017) and Vela X-1 (Sander et al. 2018). It is also hinted in the slope of Γ_{rad} shown in our demonstration model from Sander et al. (2015). While the β -law implies that Γ_{rad} asymptotically reaches a maximum value, the CMF calculations show that Γ_{rad} can decrease in the outer wind. This is more subtle in the OB models, but quite prominent in the WR models presented

Table B1. Analytic fit for the radiative acceleration and the force multiplier

	Γ_{rad}		\mathcal{M}	
	shape	detailed	shape	detailed
γ_0	1.6860	1.6397	4.3956	4.5850
γ_1	0.3206	0.3596	1.5917	1.6429
γ_2	0.4139	0.8629	5.0803	3.9346
γ_3	0.9880	1.3064	6.8170	5.7556
γ_4		-0.0481		1.2600
γ_5		0.4051		2.8576
γ_6		-0.0570		1.1911
γ_7		-0.5899		-0.5528
γ_8		-0.2478		0.2333
γ_9		-0.5414		-1.7546
γ_{10}		-0.4671		-2.1131

in this work. Plotting the force multiplier versus the velocity gradient in the lower panel of Fig. A3 reveals how complex the interplay between the two quantities really is. Even if we account only for the section outwards of $\tau_F = 2/3$, i.e. the area we concern as optically thin for driving, $\log \mathcal{M}$ is clearly a non-monotonic function of $\log \frac{dv}{dr}$, thus spoiling any mCAK description of the radiative force.

APPENDIX B: THE CHALLENGE TO DESCRIBE THE RADIATIVE ACCELERATION

In this section we illustrate the complexity of deriving an analytical approximation of the radiative acceleration for cWR stars using our WNE model from Table 1. We aim at reproducing the general shape of $\Gamma_{\text{rad}}(r)$ as a kind of blueprint for dealing with WR-type winds in situations where a detailed CMF-based calculation is not feasible, e.g. due to computational limitations in multi-dimensional or time-dependent models. Caution is advised when adopting these recipes as their parameters depend significantly on the individual stellar parameters such as T_* , L , M , and the chemical composition.

In order to not be too dependent on the particular dimensions of our archetypical model, we do not fit Γ_{rad} directly on the standard radius scale, but instead introduce the dimensionless quantity

$$x := 1 - \frac{R_*}{r} \quad (\text{B1})$$

which is well known as the kind of ‘radikand’ from the β -velocity law (i.e. $v(x) = v_\infty x^\beta$). It essentially maps our interval $r \in [R_*, \infty[$ to $x \in [0, 1[$. We then fit $\Gamma_{\text{rad}}(x)$ with a series of shifted Legendre polynomials, which provide an orthogonal basis on our interval. While Krtićka & Kubát (2011) used this technique to constrain an improved description for the wind velocity profile of O-type stars (including central stars of planetary nebulae), we apply it here to the radiative force itself. Thus we can write Γ_{rad} as a series

$$\Gamma_{\text{rad}}(x(r)) = \sum_{i=0}^n \gamma_i \tilde{P}_i(x(r)) \quad (\text{B2})$$

with the shifted Legendre polynomials $\tilde{P}_i(x)$ and the coefficients γ_i . The shifted Legendre Polynomials follow from the ordinary Legendre Polynomials $P_i(x)$ via $\tilde{P}_i(x) = P_i(2x - 1)$.

Instead of fitting Γ_{rad} , one could also take a look at the so-called *force multiplier* introduced by Castor et al. (1975)

$$\mathcal{M} := \frac{\Gamma_{\text{lines}}}{\Gamma_e} = \frac{\Gamma_{\text{rad}} - \Gamma_{\text{cont}}}{\Gamma_e}, \quad (\text{B3})$$

describing the effect of line-driving as a depth-dependent ‘boost

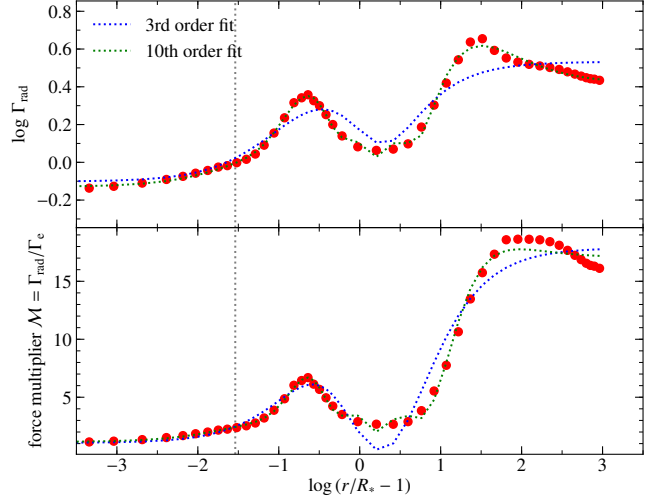


Figure B1. Stratification for Γ_{rad} (upper panel) and the force multiplier \mathcal{M} (lower panel) in the consistent WN model at Z_\odot (see Table 1 for detailed parameters). In each panel, two fits with shifted Legendre Polynomials are shown, giving either a rough representation of the curve or a detailed fit.

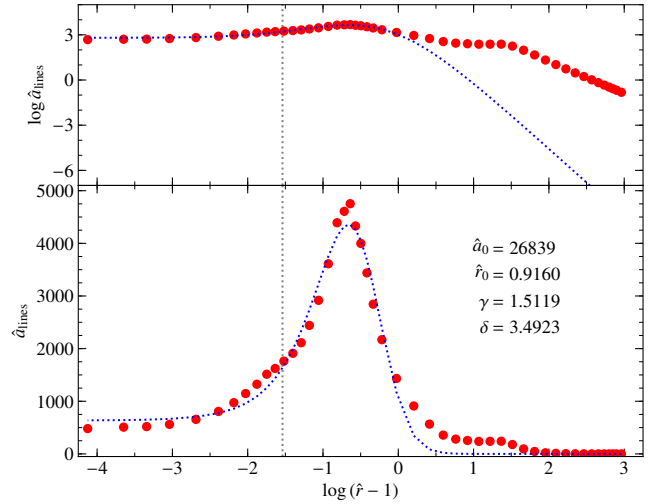


Figure B2. Line acceleration of the WN model from Table 1 in the dimensionless from suggested by Müller & Vink (2008), shown on linear (lower panel) and logarithmic (upper panel) scale. The best fit according to Eq. (B4) is shown as a blue dashed line, compared to the HD model in red.

factor’ to Γ_e . Stratifications for both, Γ_{rad} and \mathcal{M} are shown in Fig. B1 including fits with shifted Legendre Polynomials. It becomes clear that the stratifications are quite complex and a high number of orders is required to successfully reproduce the shapes. The 10th order fits given in the figures have coefficients listed in Table B1. In addition, a much simpler 4th-order representation is provided as well. While this does not represent the precise shape of the curves, it is the lowest order fit that contains all the major features of a WR-like behavior and could be useful for qualitative studies.

Using the Monte Carlo approach, Müller & Vink (2008) introduced a semi-analytical description of the radiative acceleration that is more physically motivated than a polynomial. (See Sect. 2.4 in Müller & Vink 2008, for a detailed discussion of the motivation.)

Their description for the line contribution has the form

$$\hat{a}_{\text{lines}}(\hat{r}) = \frac{\hat{a}_0}{r^{1+\delta}} \left(1 - \frac{\hat{r}_0}{\hat{r}}\right)^\gamma \quad (\text{B4})$$

with the four free parameters \hat{a}_0 , \hat{r}_0 , γ , and δ . $\hat{a}_{\text{lines}} = a_{\text{lines}} R_* a_s^{-2}$ is the total line acceleration, normalized into a dimensionless form, and $\hat{r} = r/R_*$ is simply the radius in units of R_* . In their models, the wind is isothermal, i.e. $a_s = \text{const.}$, which is not the case here. Nonetheless, we can calculate the corresponding values for \hat{a}_{lines} and perform a numerical fit for our WNE model in order to check how accurate the line acceleration of a cWR star can be reproduced by a description in the form of Eq. (B4). The result is shown in Fig. B2, where we also display the parameter set of the best fit. Looking at the lower panel, the result is quite promising at first glance, but the logarithmic scale in the upper panel reveals that the description is off by orders of magnitude in the outer wind. The reason is that Eq. (B4) permits only one local maximum and no local minima for \hat{a}_{lines} , meaning it cannot handle more than one bump. A closer inspection also shows that the increase of the acceleration just below the critical point is underestimated.

Despite the shortcomings, our fit result with the recipe from Müller & Vink (2008) is promising. Their recipe has been successfully applied for predictions of OB star winds (e.g. Muijres et al. 2012), where not as many different ionization stages contribute as in WR winds. A full physically meaningful analytic representation of the radiative acceleration will likely require an extension of the model from Müller & Vink (2008) as well as a detailed mapping of the whole WR parameter range with hydrodynamically consistent models. This is beyond the scope of the present paper, but a sufficient description of the wind acceleration of cWR and other He stars marks an important scientific goal with implications to other astrophysical fields on a likely mid- to long-term timescale.

APPENDIX C: ADDITIONAL TABLES

This paper has been typeset from a $\text{\TeX}/\text{\LaTeX}$ file prepared by the author.

Table C1. Parameters for the WR models with $\log \dot{M} = -5.15$ at different metallicities

$\log Z/Z_\odot$	$\log L/M$	$\Gamma_e(R_*)$	v_∞	$T_{2/3}^{\text{Ross}}$	$T_e(R_{\text{crit}})$
<i>WN models</i>					
1.0	4.07	0.17	4746	122	214
0.7	4.10	0.19	3579	119	204
0.3	4.20	0.24	2375	109	200
0.0	4.27	0.29	1640	92	195
-0.3	4.37	0.36	1391	80	194
-0.7	4.45	0.43	1165	75	193
-1.0	4.51	0.50	1063	74	191
-1.3	4.56	0.56	1029	75	192
-2.0	4.66	0.70	1048	81	180
-3.0	4.72	0.81	1099	83	169
-4.0	4.74	0.85	1106	83	165
-5.0	4.74	0.86	1113	83	165
-6.0	4.75	0.86	1117	83	165
<i>WC models</i>					
1.0	4.09	0.15	4351	123	212
0.7	4.16	0.17	3446	122	205
0.3	4.25	0.21	2277	114	199
0.0	4.34	0.27	2120	113	197
-0.3	4.42	0.32	1573	98	191
-1.0	4.51	0.39	1169	75	189
-1.3	4.55	0.43	1151	77	188
-2.0	4.65	0.54	1291	87	181
-2.7	4.69	0.59	1262	86	178
-3.0	4.70	0.60	1282	87	178
-3.3	4.70	0.61	1228	87	177
-3.7	4.71	0.62	1214	88	176
-4.0	4.72	0.64	1325	90	174
-4.3	4.71	0.62	1228	87	177
-5.0	4.71	0.63	1313	88	174

Table C2. Overview of the number of levels and line transitions used in the radiative transfer calculations. Nitrogen was only included for the WN models and is thus marked by an asterisk. The number of lines refers to the transitions considered in the radiative transfer. For collisions, also radiatively forbidden transitions are taken into account. The atom listed as Fe here is a generic element that also includes Sc, Ti, V, Cr, Mn, Co, and Ni. For details, see [Gräfener et al. \(2002\)](#)

Ion		Levels	Lines	Ion		Levels	Lines
He	I	35	271	P	III	10	11
He	II	26	325	P	IV	10	8
He	III	1	0	P	V	10	20
C	II	3	2	P	VI	1	0
C	III	40	226	S	III	10	7
C	IV	25	230	S	IV	25	54
C	V	1	0	S	V	10	13
N*	I	3	2	S	VI	22	75
N*	II	38	201	S	VII	1	0
N*	III	30	94	Cl	III	1	0
N*	IV	38	154	Cl	IV	24	34
N*	V	20	114	Cl	V	18	29
N*	VI	1	0	Cl	VI	23	46
O	II	36	146	Cl	VII	1	0
O	III	33	121	Ar	II	10	9
O	IV	29	76	Ar	III	30	63
O	V	36	153	Ar	IV	13	20
O	VI	16	101	Ar	V	10	11
O	VII	1	0	Ar	VI	9	11
Ne	II	10	9	Ar	VII	20	34
Ne	III	18	18	Ar	VIII	11	24
Ne	IV	35	159	Ar	IX	10	10
Ne	V	54	263	Ar	X	3	1
Ne	VI	49	239	K	III	10	12
Ne	VII	36	229	K	IV	23	27
Ne	VIII	77	517	K	V	19	33
Ne	IX	23	51	K	VI	28	38
Ne	X	15	25	K	VII	8	6
Ne	XI	1	0	K	VIII	1	0
Na	III	1	0	Ca	III	10	7
Na	IV	10	9	Ca	IV	24	43
Na	V	10	14	Ca	V	15	12
Na	VI	10	13	Ca	VI	15	17
Na	VII	1	0	Ca	VII	10	9
Mg	III	10	12	Ca	VIII	1	0
Mg	IV	10	9	Fe	III	1	0
Mg	V	10	9	Fe	IV	18	77
Mg	VI	10	19	Fe	V	22	107
Mg	VII	1	0	Fe	VI	29	194
Al	III	10	18	Fe	VII	19	87
Al	IV	10	10	Fe	VIII	14	49
Al	V	10	9	Fe	IX	15	56
Al	VI	10	9	Fe	X	28	170
Al	VII	1	0	Fe	XI	26	161
Si	II	10	13	Fe	XII	13	37
Si	III	10	9	Fe	XIII	15	50
Si	IV	10	22	Fe	XIV	14	49
Si	V	10	9	Fe	XV	10	25
Si	VI	10	9	Fe	XVI	9	20
Si	VII	1	0	Fe	XVII	1	0
Si	VIII	1	0				